

Reflection in Seyfert galaxies and the unified model of AGN

C. Ricci^{1,2}, R. Walter^{1,2}, T. J.-L. Courvoisier^{1,2}, and S. Paltani^{1,2}

¹ ISDC Data Centre for Astrophysics, University of Geneva, ch. d’Ecogia 16, 1290 Versoix, Switzerland

² Geneva Observatory, University of Geneva, ch. des Maillettes 51, 1290 Versoix, Switzerland

Received; accepted

ABSTRACT

We present a deep study of the average hard X-ray spectra of Seyfert galaxies. We aim to test the unified model of active galactic nuclei, and constrain differences and similarities between different classes of objects. We analyzed all public *INTEGRAL* IBIS/ISGRI data available on all the 165 Seyfert galaxies detected at $z < 0.2$. Our final sample consists of 44 Seyfert 1s, 29 Seyfert 1.5s, 78 Seyfert 2s, and 14 narrow-line Seyfert 1s. For each subsample, we stacked all the images, and derived their average hard X-ray spectra in the 17–250 keV energy range. We performed a detailed spectral analysis using both a model-independent and a model-dependent approach. All classes of Seyfert galaxies show on average the same nuclear continuum, as foreseen by the zeroth order unified model, with a cutoff energy of $E_C \gtrsim 200$ keV, and a photon index of $\Gamma \simeq 1.8$. The average optical depth of the Comptonizing medium is consistent for the different classes ($\tau \simeq 0.8$). Compton-thin Seyfert 2s show a reflection component stronger than Seyfert 1s and Seyfert 1.5s. Most of this reflection is due to mildly obscured ($10^{23} \text{ cm}^{-2} \leq N_H < 10^{24} \text{ cm}^{-2}$) Seyfert 2s, which have a significantly stronger reflection component ($R = 2.2^{+4.5}_{-1.1}$) than Seyfert 1s ($R \leq 0.4$), Seyfert 1.5s ($R \leq 0.4$) and lightly obscured ($N_H < 10^{23} \text{ cm}^{-2}$) Seyfert 2s ($R \leq 0.5$). This cannot be explained easily by the unified model. The absorber/reflector in mildly obscured Seyfert 2s might cover a large fraction of the X-ray source, and contain clumps of Compton-thick material. The large reflection found in the spectrum of mildly obscured Seyfert 2s reduces the amount of Compton-thick objects needed to explain the peak of the cosmic X-ray background. Our results are consistent with the fraction of Compton-thick sources being $\sim 10\%$. The spectra of Seyfert 2s with and without polarized broad lines do not show significant differences, the only difference between the two samples being the higher hard X-ray and bolometric luminosity of Seyfert 2s with polarized broad lines. The average hard X-ray spectrum of narrow-line Seyfert 1s is steeper than those of Seyfert 1s and Seyfert 1.5s, probably due to a lower energy of the cutoff.

Key words. Galaxies: Seyferts – X-rays: galaxies – Galaxies: active – Galaxies: nuclei – X-rays: diffuse background

1. Introduction

Active Galactic Nuclei (AGN) emit over the entire electromagnetic spectrum, and are commonly assumed to be powered by accretion onto a super massive black hole (Rees 1984). Seyfert galaxies host AGN, and are classified according to their emission lines as Seyfert 1s (Sy1s, showing broad and narrow emission lines), and Seyfert 2s (Sy2s, showing only narrow lines). Many Seyfert galaxies exhibit optical spectra with properties in-between those of Sy1 and Sy2 galaxies (e.g., Osterbrock & Koski 1976). These objects have been classified as type 1.2, 1.5, 1.8, or 1.9 Seyfert galaxies, depending on the details of their optical spectra. Studies of the optical spectra of Seyfert 2 galaxies using polarized light (Miller & Antonucci 1983, Antonucci & Miller 1985) showed that broad emission lines can also be detected in some of these objects, and led to the development of the so-called unified model (UM, Antonucci, 1993). According to this model, the same engine is at work in all kind of Seyfert galaxies, and the differences between Seyfert 1s and Seyfert 2s can be ascribed solely to orientation effects and to anisotropic obscuration. In this model, the line of sight to the nucleus is (Seyfert 2s) or is not (Seyfert 1s) obstructed by optically thick material, possibly distributed in a toroidal geometry. X-ray observations have confirmed this idea, showing that most AGN unabsorbed in X-rays are of the optical Seyfert 1 type, and that

most AGN that are absorbed belong to the Seyfert 2 group (e.g., Awaki et al. 1991).

However, in the past few years observational evidence of significant differences between Seyfert 1s and Seyfert 2s has been discovered. Seyfert 1s with significant absorption have been found (e.g., Fiore et al. 2001, Cappi et al. 2006), along with Seyfert 2s without X-ray absorption (e.g., Pappa et al. 2001, Panessa & Bassani 2002). Furthermore, spectropolarimetric surveys indicate that only $\sim 30 - 50\%$ of Seyfert 2s have polarized broad lines (PBLs), which might imply that not all of them harbor hidden BLRs (e.g., Tran 2001, 2003, Gu & Huang 2002). In the soft X-rays the photon index distribution is found to be skewed towards low values of Γ for obscured objects (Brightman & Nandra 2010), while in the hard X-rays, Seyfert 2s have been found to have harder spectra than Seyfert 1s (e.g., Zdziarski et al. 1995, Malizia et al. 2003, Deluit & Courvoisier 2003, Ajello et al. 2008a, Burlon et al. 2011).

Two subclasses of objects cannot be easily explained by the unified model: narrow-line Seyfert 1s (NLS1s) and low ionization nuclear emission line regions (LINERs). It has been suggested that NLS1s are AGN in their early phase (Grupe et al. 1999), characterized by relatively low black hole masses (e.g., Grupe & Mathur 2004) and very high accretion rates in terms of Eddington units (e.g., Grupe et al. 2010). LINERs (Heckman 1980) are low luminosity AGN, and display multiwavelength peculiar characteristics. They could be the link between AGN and normal galaxies (Zhang et al. 2009, Rovilos et al. 2009), or their

SMBH might accrete differently from normal Seyfert galaxies (Ho 2008).

The X-ray emission of Seyfert galaxies is thought to be produced by the Comptonization of ultraviolet (UV) photons generated in the innermost edge of the accretion disk by a population of hot electrons located in a coronal region sandwiching the disk (Haardt & Maraschi 1991, 1993). The X-ray spectrum of AGN can be normally well described by a power law model with a photon index between $\Gamma \simeq 1.8$ (e.g., Dadina et al. 2008) and $\Gamma \simeq 2$ (e.g., Beckmann et al. 2009). Other common characteristics are an exponential cutoff at an energy depending on the temperature of the plasma T_e and its Thomson opacity, and photoelectric absorption at low energies, caused by material along the line of sight. Two prominent features generated by the reflection of the continuum are also observed in the X-ray spectra of AGN: a neutral iron $K\alpha$ line (at 6.4 keV in the local reference frame) and a reflection hump peaking at $E \simeq 30$ keV (Magdziarz & Zdziarski 1995). At energies $\gtrsim 20$ keV, the photoelectric cross-section sharply declines, and the presence of matter along the line of sight does not play a significant role, unless the source is Compton-thick (CT; $N_{\text{H}} > 1.5 \times 10^{24} \text{ cm}^{-2}$). Therefore hard X-rays are ideal for probing the intrinsic emission of AGN and testing the UM, according to which different types of Seyfert galaxies should show on average the same characteristics.

The *International Gamma-Ray Astrophysics Laboratory* (*INTEGRAL*; Winkler et al. 2003) is a hard X-ray/soft γ -ray mission, designed for imaging and spectroscopy with high angular and spectral resolution in the energy range from ~ 3 keV to 10 MeV. Since its launch on October 17, 2002, the soft γ -ray imager IBIS/ISGRI (15–1000 keV; Lebrun et al. 2003, Ubertini et al. 2003) on board *INTEGRAL* has detected more than 200 AGN, among which about 90 were detected for the first time in the hard X-rays. IBIS/ISGRI uses the coded-aperture technique (Caroli et al. 1987) and has a large field of view of 29° square with a spatial resolution of 12 arcmin.

We present a very deep study of the average hard X-ray spectra of Seyfert galaxies. Our main aim is to test the unified model by studying the average hard X-ray emission of different types of radio-quiet AGN detected by *INTEGRAL* IBIS/ISGRI, and to constrain the average spectral characteristics of each class. We also investigate whether Seyfert 2s showing (hereafter PBL Sy2s) and not showing (hereafter NPBL Sy2s) PBLs are intrinsically similar objects or not. In Sect. 2, we present the sample of AGN; in Sect. 3, we describe how the data analysis was performed and how the hard X-ray spectra were obtained; in Sect. 4, we present the results obtained from a model-independent analysis of the spectra, and in Sect. 5, we discuss the model-dependent spectral analysis. We study the origin of a strong reflection component found in the spectrum of Seyfert 2s in Sect. 6; and in Sect. 7, we discuss our results and their implications for the UM and the cosmic X-ray background (CXB). In Sect. 8, we present our conclusions and summarize our findings.

2. The sample

The sample consists of all the 205 Seyfert galaxies detected (significance $> 5\sigma$) in the hard X-rays by *INTEGRAL* IBIS/ISGRI during its first eight years of operations. We considered as their optical classifications the ones reported in the latest version of the Veron Catalog of Quasars and AGN (Veron-Cetty & Veron, 2010).

The sample consists of 38 Seyfert 1s, 17 Seyfert 1.2s, 34 Seyfert 1.5s, 3 Seyfert 1.8s, 15 Seyfert 1.9s, 75 Seyfert 2s, 8

LINERs, and 15 NLS1s. We excluded from these subsamples the LINERs, because the physical characteristics of their accretion flow might differ from those of the others. We grouped Seyfert 1.2s with Seyfert 1s, and both Seyfert 1.8s and Seyfert 1.9s with Seyfert 2s because of their similarity.

2.1. The role of absorption

To model the effect of absorption on the X-ray spectra of AGN, one has to take into account both photoelectric absorption and Compton scattering. The photoelectric cross-section σ_{ph} has a strong dependence on the energy, while Compton scattering in the hard X-rays depends on the Thomson cross-section σ_{T} , and is constant with energy up to the Klein-Nishina decline. The cumulative effect of the two cross-sections is given by

$$M(E) = e^{-\sigma_{\text{ph}}(E)N_{\text{H}}} \times e^{-\sigma_{\text{T}}N_{\text{H}}}. \quad (1)$$

For column densities of the order of $\sigma_{\text{T}}^{-1} = 1.5 \times 10^{24} \text{ cm}^{-2}$, only about 30% of the flux is able to escape at ~ 20 keV (see Fig. 1). About 60% of the original emission is unabsorbed for $N_{\text{H}} = 7 \times 10^{23} \text{ cm}^{-2}$, and we used this value as a threshold between Compton-thin and Compton-thick sources. Thus, we included in our final sample of Seyfert 2s only the objects with a value of column density of $N_{\text{H}} \leq 7 \times 10^{23} \text{ cm}^{-2}$, and placed the 10 Seyfert 2s with $N_{\text{H}} > 7 \times 10^{23} \text{ cm}^{-2}$ in the CT Seyfert 2s sample. We note, however, that none of the sources in our sample has a N_{H} in the $(7\text{--}10) \times 10^{23} \text{ cm}^{-2}$ range, so in the following we refer to 10^{24} cm^{-2} as the threshold between Compton-thin and Compton-thick objects. In the following, we use solar abundances and the photoelectric cross section of Morrison and McCammon (1983).

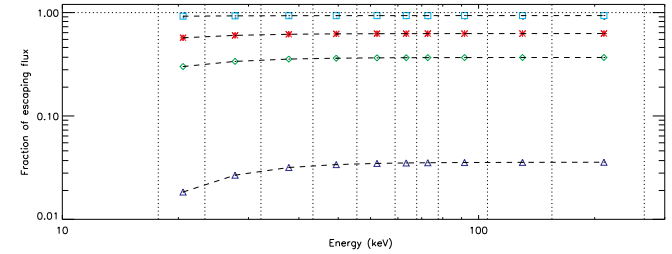


Fig. 1. Fraction of escaping flux in the 10 energy bins used. Squares represent $N_{\text{H}} = 10^{23} \text{ cm}^{-2}$, stars $N_{\text{H}} = 7 \times 10^{23} \text{ cm}^{-2}$, diamonds $N_{\text{H}} = 1.5 \times 10^{24} \text{ cm}^{-2}$, and triangles $N_{\text{H}} = 5 \times 10^{24} \text{ cm}^{-2}$.

2.2. Excluded sources

To avoid contamination and problems related to the way we obtain the average spectra (see Sect. 3), we excluded from the sample 10 sources which are too close ($\leq 0.4^\circ$) to each other or to other bright sources. We excluded 11 sources with redshift $z > 0.2$ to avoid spurious effects due to redshifted spectral features (i.e. the high-energy cutoff and the reflection hump). We removed the 5 sources detected with a significance $> 50\sigma$, to prevent them from dominating the final spectra.

Four sources with either an uncertain classification or peculiar absorbers were also excluded from the analysis. Was49 is an interacting system of galaxies containing two Seyfert nuclei (Moran et al. 1992). The AGN IGR J16426+6536 shows characteristics typical of both NLS1 (Masetti et al. 2009)

Table 1. Sources detected by *INTEGRAL* IBIS/ISGRI but excluded from the analysis, and reason for their exclusion. More details can be found in Sect. 2.2.

Source	Type	Reason for the exclusion
4U 1344–60	Sy 1.5	C
Circinus Galaxy	CT Sy 2	B
ESO 138–1	Sy 2	C
ESO 383–18	Sy 2	C
GRS 1734–292	Sy 1	B
IC 4329A	Sy 1	B
IGR J00465–4005	Sy 2	R
IGR J05270–6631	Sy 1	R
IGR J06117–6625	Sy 1.5	R
IGR J09523–6231	Sy 2	R
IGR J10147–6354	Sy 1	R
IGR J12131+0700	Sy 1.5	C
IGR J13038+5348	Sy 1	R
IGR J14515–5542	Sy 2	C
IGR J16024–6107	Sy 2	C
IGR J16056–6110	Sy 1.5	C
IGR J16426+6536	NLS1	U
IGR J17476–2253	Sy 1	C
IGR J17488–3253	Sy 1	C
IGR J18249–3243	Sy 1	R
IGR J21272+4241	Sy 2	R
NGC 1365	Sy 2	U
NGC 4151	Sy 1.5	B
NGC 4388	Sy 2	B
NGC 4939	Sy 2	U
NGC 6221	Sy 2	C
PKS 0637–752	Sy 1.5	R
QSO B1821+643	Sy 1	R
SWIFT J0216.3+5128	Sy 2	R
Was 49a + Was 49b	Sy 1 + Sy 2	U

Notes. C: close to other detected sources ($\leq 0.4^\circ$); U: classification unclear or with particular characteristics; R: $z > 0.2$; B: bright (detection significance $> 50\sigma$ in the 17–80 keV band).

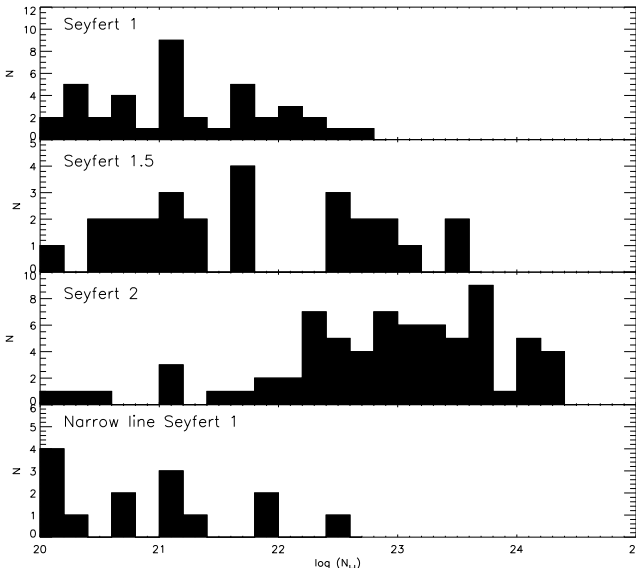


Fig. 2. Hydrogen column density distributions of Seyfert 1s, Seyfert 1.5s, Seyfert 2s and narrow-line Seyfert 1s.

and Seyfert 1.5 (Butler et al. 2009) galaxies. The Seyfert 1.8 NGC 1365 has been found to undergo transitions from a “transmission dominated” to a “reprocessing dominated” state and back in a few weeks time, which have been interpreted as due to eclipses of CT material along the line of sight (Risaliti et al. 2005). A similar state transition has been observed in NGC 4939 (Guainazzi et al. 2005), a Seyfert 2 that was previously classified as Compton-thick by *BeppoSAX* observations (Maiolino et al. 1998). The excluded sources are reported in Table 1.

2.3. The final sample

The final sample used for the analysis consists of 165 AGN, of which 44 are Seyfert 1s, 29 Seyfert 1.5s, 68 Compton-thin Seyfert 2s, 10 CT Seyfert 2s, and 14 NLS1s. Spectropolarimetric data are available for only 19 of the 68 Compton-thin Seyfert 2s of our sample. Among these, 11 show and 8 do not show PBLs. The sources and their characteristics are reported in Appendix A.

Figure 2 shows the distribution of the column density for the different classes of AGN. The average values of the column densities of the different classes are $N_H^{Sy1} = 5.4 \times 10^{21} \text{ cm}^{-2}$, $N_H^{Sy1.5} = 3.7 \times 10^{22} \text{ cm}^{-2}$, $N_H^{Sy2} = 1.5 \times 10^{23} \text{ cm}^{-2}$, $N_H^{NLS1} = 1.9 \times 10^{21} \text{ cm}^{-2}$, and $N_H^{CT} = 1.5 \times 10^{24} \text{ cm}^{-2}$, for Seyfert 1s, Seyfert 1.5s, Seyfert 2s, NLS1s, and CT Seyfert 2s, respectively. These values agree with the paradigm that Seyfert 2s are more obscured than Seyfert 1s and Seyfert 1.5s. Considering the average column densities of the different samples, the percentage of flux absorbed in the first band (17–22 keV) by photoelectric processes is about 0.01%, 0.5%, and 2% for Seyfert 1s, Seyfert 1.5s, and Seyfert 2s, respectively. Compton processes have a stronger influence at these energies, and the fraction of scattered flux is of 0.3%, 2.4% and 9.5%, for Seyfert 1s, Seyfert 1.5s and Seyfert 2s, respectively. In the case of CT Seyfert 2s, the influence of the obscuring material is stronger and $\simeq 18\%$ of the flux is photoelectrically absorbed, whereas when we also consider Compton scattering, only $\simeq 30\%$ of the flux escapes. A Kolmogorov-Smirnov (KS) gives a probability of $\simeq 67\%$ that the column density distributions of Seyfert 1s and Seyfert 1.5s are drawn from the same parent population. The probability is much lower when comparing NLS1s to Seyfert 1s and Seyfert 1.5s ($\simeq 10\%$).

In Fig. 3, we show the redshift distribution of our final sample. The average value of the redshift is $z=0.03$, and the average detection significance is 12.7σ .

In Fig. 4, we show the luminosity distributions in the 17–80 keV band of our samples of Seyfert galaxies. The luminosities were calculated assuming a standard Λ CDM cosmological model, Crab-like spectra (e.g., Jourdain & Roques 2009), and $H_0 = 70 \text{ km s}^{-1} \text{ Mpc}^{-1}$. The average values of the luminosity are $L_{Sy1} = 5.0 \times 10^{43} \text{ erg s}^{-1}$, $L_{Sy1.5} = 3.7 \times 10^{43} \text{ erg s}^{-1}$, $L_{Sy2} = 2.1 \times 10^{43} \text{ erg s}^{-1}$, $L_{CTS} = 8.3 \times 10^{42} \text{ erg s}^{-1}$, and $L_{NLS1} = 1.7 \times 10^{43} \text{ erg s}^{-1}$, for Sy1s, Sy1.5s, Sy2s, CT Sy2s, and NLS1s, respectively. The luminosity of CT Sy2 was corrected for Compton scattering. A KS test gives a probability of $\simeq 53\%$ that the luminosity distributions of Seyfert 1s and Seyfert 1.5s are statistically compatible. The probability is much lower when comparing Seyfert 1s to Seyfert 2s ($\simeq 2\%$), and Seyfert 1s to NLS1s ($\simeq 10\%$).

3. INTEGRAL IBIS/ISGRI data analysis

We used all the public data obtained by *INTEGRAL* IBIS/ISGRI as of May 2010, for a total of more than 50 thousands pointings or “science windows” (SCWs). The typical exposure time

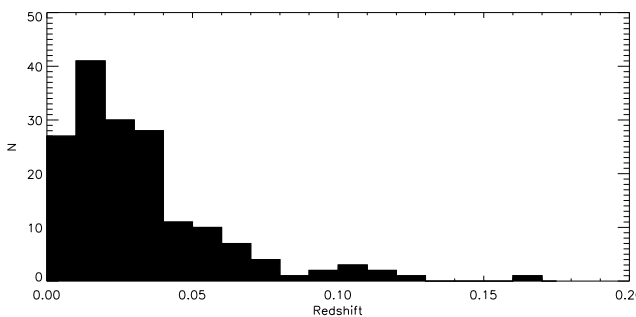


Fig. 3. Redshift distribution of our final sample of *INTEGRAL* IBIS/ISGRI detected Seyfert galaxies.

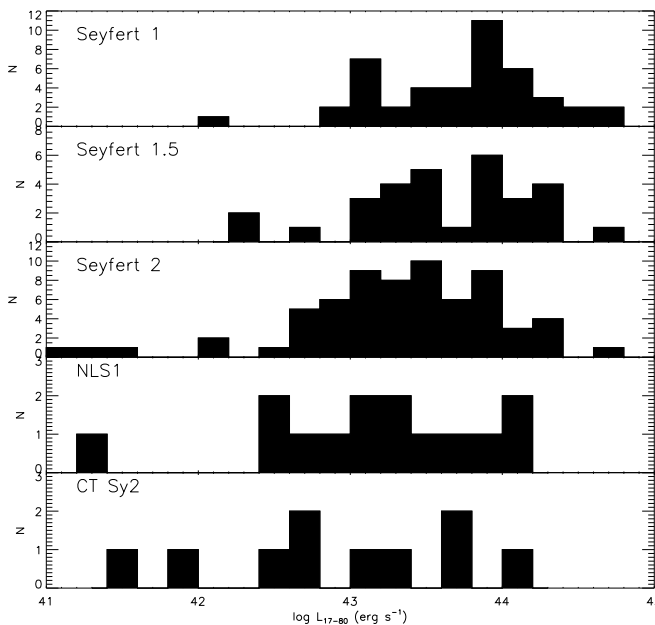


Fig. 4. Luminosity distribution of Seyfert 1s, Seyfert 1.5s, Compton-thin Seyfert 2s, NLS1s, and CT Sy2s in the 17–80 keV band.

of these pointings is of $(1 - 3) \times 10^3$ s. Several thousand pointings, including at least one source of the sample in its field of view and with an effective exposure longer than 120 s were selected, spanning times between December 30, 2002 (revolution 26) and April 7, 2009 (revolution 791).

The *ISGRI* data were reduced using the *INTEGRAL* Offline Scientific Analysis software¹ version 9.0, publicly released by the ISDC Data Centre for Astrophysics (Courvoisier et al. 2003).

Individual sky images for each pointing were produced in a broad energy band (17–250 keV), and divided into ten bins as follows: 17–22, 22–30, 30–40, 40–51, 51–63, 63–71, 71–80, 80–105, 105–150, and 150–250 keV.

To extract the average spectra of the different AGN samples, we followed the procedure adopted by Walter & Cabral (2009). We created 500×500-pixels mosaic images modifying the coordinate system of each individual image, setting the coordinates of each source of the sample to an arbitrary fixed position ($\alpha=0$, $\delta=0$). The geometry of the image was also modified to have a consistent PSF independently of the position of the source in the

Table 2. Number of sources (1), effective exposures (2), detection significances (3), and count rates (4) of the different samples. All the values refer to the 17–80 keV band.

Sample	(1) Srcs	(2) Exp. [Ms]	(3) Det. Significance [σ]	(4) Ct rate [ct/s]
Seyfert 1	44	37.6	91.1	0.396 ± 0.004
Seyfert 1.5	29	13.2	59.1	0.429 ± 0.007
Seyfert 2	68	44.0	102.8	0.390 ± 0.004
CT Sy2	10	4.7	32.9	0.405 ± 0.012
NLS1	14	10.1	44.3	0.377 ± 0.008
MOB Sy2	27	13.8	59.6	0.430 ± 0.007
LOB Sy2	34	23.4	78.1	0.424 ± 0.006
PBL Sy2	11	4.2	99.0	1.301 ± 0.013
NPBL Sy2	8	2.9	31.2	0.479 ± 0.015

field of view (FOV). These mosaic images provide a stack of all the selected IBIS/ISGRI data for each considered sample.

To minimize the systematics in the mosaic images, we excluded 1455 individual sky images (many obtained before revolution 38, when the IBIS bottom anti-coincidence was reconfigured) that had a background fluctuation rms larger than 1.1σ in the significance image, and 779 images with a minimum significance smaller than -5.5σ . In addition to these, we excluded 627 images taken when the ISGRI was in staring mode. A total of 56,611 images were finally included in the processing (some of them many times, when including several sources). All known ISGRI sources with significance above 5σ were used for image cleaning. When known accurately, the position of these sources was fixed to catalogue values taken from the *INTEGRAL* general reference catalog (Ebisawa et al. 2003)².

The mosaic images were built with a tangential projection using a factor of two oversampling when compared to the individual input sky images, this results in a pixel size of 2.4 arcmin at the center of the mosaic. The photometric integrity and accurate astrometry were obtained by calculating the intersection between input and output pixels, and weighting the count rates according to the overlapping area.

The average signal extracted in the large 17–80 keV band from each ISGRI mosaic, and both the exposures and the number of sources used are reported in Table 2. The detection significances in the 17–80 keV band range between 102.8σ and 32.9σ , for the largest and smallest sample (i.e. Seyfert 2s and CT Sy2s), respectively. The effective exposure obtained at the center of the mosaics are between 4.7 Ms (for CT Sy2s) and 44.0 Ms (for Seyfert 2s).

The ten-bin spectra of the final samples were extracted from the images in the 10 narrow bands using `mosaic_spec`. In all spectra, the highest energy bin (i.e. 150–250 keV) has a low significance ($\sim 2.5 - 3\sigma$), but we use it for the sake of completeness. We used the latest detector response matrix (RMF), and calculated the ancillary response matrices (ARFs) of each sample with a weighted average of the nine available ARFs, based on the number of SCWs within the validity time of a particular ARF.

¹ <http://www.isdc.unige.ch/>

² <http://www.isdc.unige.ch/integral/science/catalogue>

4. Model-independent spectral analysis

A model-dependent spectral analysis has the drawback of possible parameter degeneracy, which might not allow us to constrain several parameters at the same time. An alternative method to characterize differences and similarities between different classes of Seyfert galaxies, independently of their average flux, is by means of a model-independent approach. This was achieved by normalizing the flux of the two different spectra in the first bin (17–22 keV), and then calculating their ratio.

4.1. Seyfert galaxies

We have no information about the value of the hydrogen column density of seven Seyfert 2s. To discard the possibility that these objects are CT, which might influence significantly the result, we calculated the ratio between the spectra of the Seyfert 2 sample including and excluding these seven objects. This ratio is fully consistent with 1.

In Fig. 5, we show the normalized spectra of Sy1s and Sy1.5s (in the upper panels) and their ratios (in the lower panel). The average spectrum of Seyfert 1s is consistent with that of Seyfert 1.5s along the whole spectrum. The ratio of the average spectrum of Seyfert 1 galaxies to the normalized one of NLS1s diverges from the unity from ~ 40 keV (Fig. 6), with the spectrum of NLS1s being steeper than that of Sy1s. Since the spectra of Seyfert 1s and Seyfert 1.5s are very similar, we merged them and compared the resulting spectrum to that of Seyfert 2s. We show in Fig. 7 the ratio obtained after normalization. The spectrum of Seyfert 2s displays a clear excess over those of the Seyfert 1s and Seyfert 1.5s of $48 \pm 8\%$ in the 22–63 keV band. This bump peaks around 40 keV, reaching 20%, and might indicate that Seyfert 2s have a stronger reflection component than Seyfert 1s and Seyfert 1.5s. At energies higher than 60 keV, the ratio is consistent with 1, indicating similar cutoff energies. The ratio of the spectra of Compton-thin to Compton-thick Seyfert 2s is consistent with one up to 150 keV (Fig. 8). Including in our sample of Sy2s the two objects excluded because of their complex absorption does not affect the results, and the ratio between the spectra with and without these sources is consistent with one.

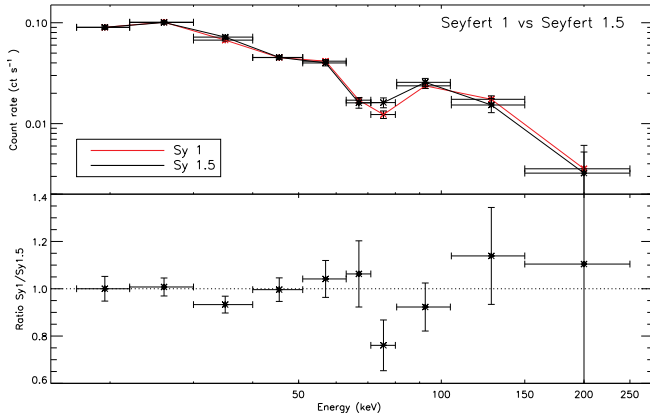


Fig. 5. Normalized spectra (upper panel) and ratio (lower panel) of Seyfert 1s to Seyfert 1.5s.

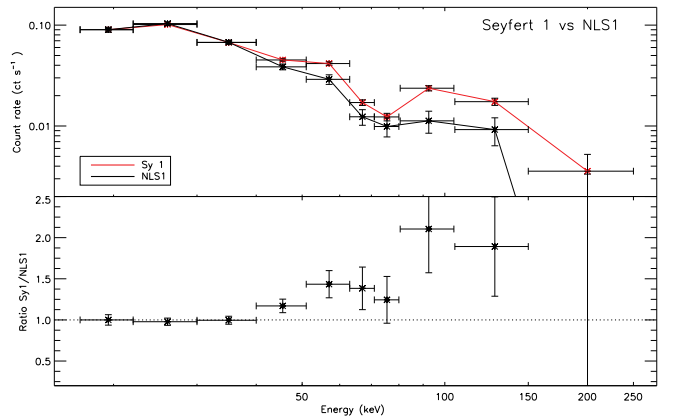


Fig. 6. Normalized spectra (upper panel) and ratio (lower panel) of Seyfert 1s to NLS1s.

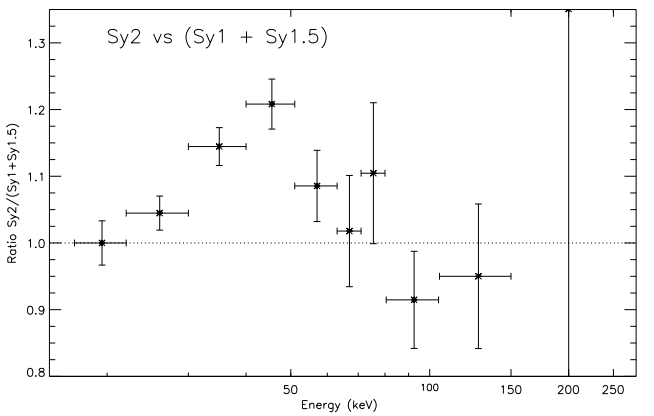


Fig. 7. Ratio between the normalized spectra of Compton-thin Seyfert 2s and that of both Seyfert 1s and Seyfert 1.5s.

4.2. Lightly obscured and mildly obscured Seyfert 2s

The Seyfert 2s contained in our sample appear to have characteristics that differ significantly from those of Seyfert 1 and Seyfert 1.5 galaxies. To test whether absorption might still play a role in the hard X-ray spectra of Compton-thin Seyfert 2 galaxies, we divided the sample into two subsamples, one including the objects with $10^{23} \text{ cm}^{-2} \leq N_{\text{H}} < 10^{24} \text{ cm}^{-2}$ (henceforth mildly obscured Seyfert 2s, MOB Sy2s), and the other those with $N_{\text{H}} < 10^{23} \text{ cm}^{-2}$ (henceforth lightly obscured Seyfert 2s, LOB Sy2s). The MOB and LOB Sy2 samples contain 27 and 35 objects, respectively. In Table 2, we report the detection significances, exposures, and fluxes obtained for these samples. We did not consider the sources with an unknown value of N_{H} .

In Fig. 9, we show the ratio obtained by comparing the spectrum of MOB Sy2s to that of LOB Sy2s. The figure highlights significant differences between the two spectra, with the emission of MOB Sy2s being harder up to ~ 60 keV and then softer (up to ~ 150 keV) than that of LOB Sy2s. This clearly shows that the bump seen by comparing the spectrum of Seyfert 2s to those of Seyfert 1s and Seyfert 1.5s (Fig. 7) comes prevalently from the contribution of MOB Sy2s (see Fig. 10).

The spectrum of LOB Sy2s appears to be very similar to that of Seyfert 1s (Fig. 10), although an excess of $\simeq 20\%$ is evident in the 30–50 keV band. This excess might be related to a stronger reflection component in LOB Seyfert 2s than in Seyfert 1s. MOB

Sy2s present instead a spectrum similar to that of CT Sy2s, and their ratio is consistent with 1 (Fig. 10).

To test the influence of bright MOB Sy2s on their average spectrum, we compared the spectra obtained with and without the five brightest sources ($> 20\sigma$). The ratio obtained after normalizing the two spectra is fully consistent with one, from which we can conclude that the average spectrum of MOB Sy2s is not influenced by peculiar bright sources.

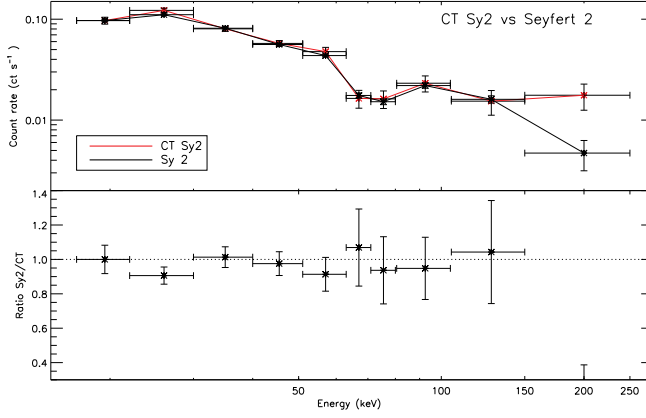


Fig. 8. Normalized spectra (upper panel) and ratio (lower panel) of Compton-thin Seyfert 2s to CT Sy2s.

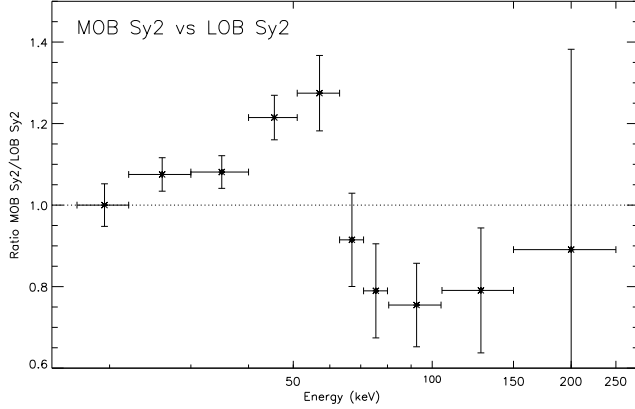


Fig. 9. Ratio of the normalized spectra of MOB to LOB Seyfert 2 galaxies.

4.3. Seyfert 2s with and without PBLs

To test whether PBL and NPBL Sy2s have different characteristics, we extracted and analyzed their average hard X-ray spectra. In Table 2, we report the detection significances, exposures, and fluxes obtained for the two samples.

Comparing the spectrum of PBL Sy2s to the one of NPBL Sy2s (Fig. 11), it is evident that the ratio is consistent with 1.

When compared to the spectrum of Seyfert 1s, the spectra of PBL and NPBL Sy2s have similar characteristics. As for the whole Seyfert 2 sample, both PBL and NPBL Sy2s display evidence of a greater reflection component. This is probably due to the contribution of the MOB Sy2s present in the samples.

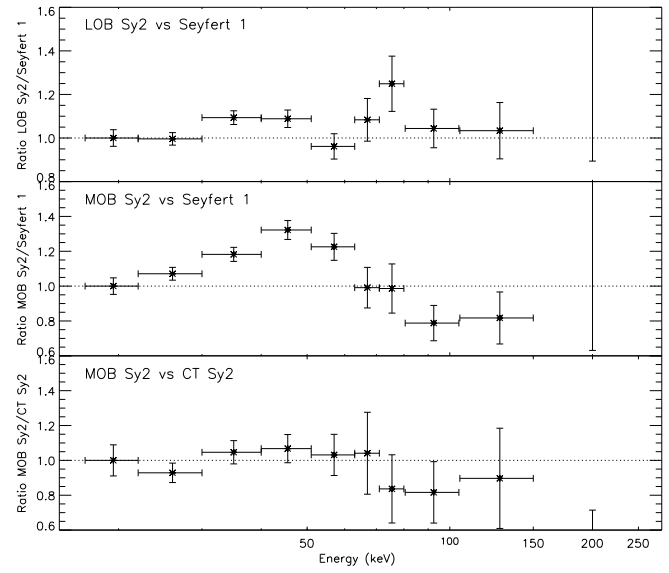


Fig. 10. Ratio between the normalized spectra of LOB Seyfert 2s and Seyfert 1s (top panel), between the spectra of MOB Seyfert 2s and Seyfert 1s (center panel), and between the spectra of MOB Seyfert 2s and CT Seyfert 2s (bottom panel).

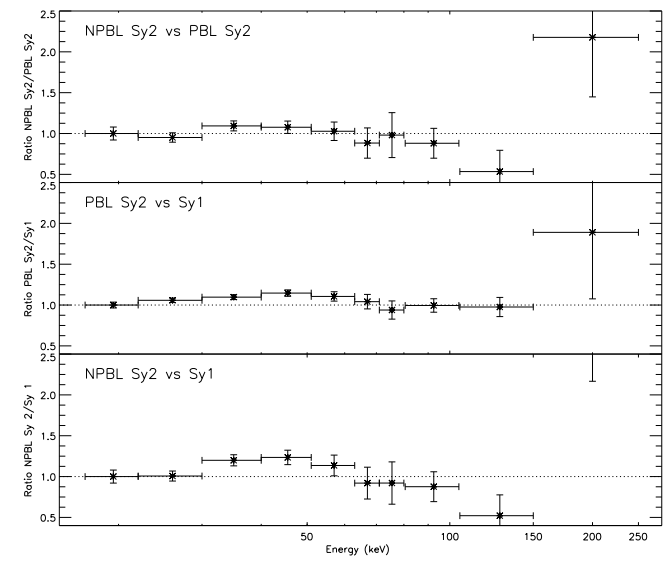


Fig. 11. Ratio between the normalized spectra of PBL and NPBL Sy2s (top panel), between Seyfert 1s and PBL (center panel), and NPBL Sy2s (bottom panel).

4.4. Comparison with a simulated power law spectrum

In Fig. 12, we show the ratios between the normalized spectra of Seyfert galaxies and a simulated power law spectrum with a photon index of $\Gamma = 1.9$. Using XSPEC (version 12.5.0, Arnaud 1996), we simulated 20 power-law spectra, using the *fakeit* command. We used the latest RMF and calculated the ARF from a weighted average of the nine available ARFs, with the weights proportional to the validity period duration of each ARF. The power law spectrum used is the average of the 20 simulated spectra, and the errors are their standard deviations.

Seyfert 1s and Seyfert 1.5s show a ratio close to unity below 100 keV, and a small excess around 30 keV, which is possibly

a signature of reflection. The excess in the 22–40 keV band is $8 \pm 3\%$ and $9 \pm 3\%$ for Seyfert 1s and Seyfert 1.5s, respectively.

The spectrum of Seyfert 2s displays a stronger excess ($27 \pm 3\%$) in the same band, and is harder than the power law up to 80 keV. Above 150 keV, the spectra of Seyfert 1s, Seyfert 1.5s and Seyfert 2s become softer than the power law; this effect might be related to the presence of a high-energy cutoff.

LOB Sy2s show an excess of $17 \pm 3\%$ over the simulated power law in the 22–40 keV band, and do not present any significant softening above 100 keV. MOB Sy2s show the most significant differences, being harder below $\simeq 60$ keV and softer above 80 keV. The excess is of $87 \pm 9\%$ in the 22–63 keV band, and of $34 \pm 5\%$ in the 20–40 keV band. A similar excess ($78 \pm 17\%$ and $36 \pm 9\%$) is found by comparing the average spectrum of CT Seyfert 2s to the simulated power law in the same bands.

To estimate the amount of curvature in the spectrum, we introduce the parameter ρ_R given by

$$\rho_R = \frac{R_{30}}{R_{80}}, \quad (2)$$

where R_{30} and R_{80} are the ratios of the normalized spectra to the power law in the 30–40 keV and 80–105 keV band, respectively. Seyfert 1s ($\rho_R = 1.09 \pm 0.07$) have a value of ρ_R consistent with those of Seyfert 1.5s ($\rho_R = 1.06 \pm 0.11$) and LOB Sy2s ($\rho_R = 1.14 \pm 0.03$). The value of this parameter is significantly larger for MOB Sy2s ($\rho_R = 1.63 \pm 0.14$), while it is $\rho_R = 1.27 \pm 0.24$ for CT Sy2s.

5. Model-dependent spectral analysis

We analyzed the average IBIS/ISGRI spectra using XSPEC. Throughout the paper, we used 3σ errors. The probabilities that additive parameters improve a fit are calculated with the F-test.

We tested simple models such as a power law, and a power law with an exponential cutoff at high energies. To account for the presence of reflection, we used the *pexrav* model (Magdziarz & Zdziarski 1995). *Pexrav* calculates the spectrum produced by an X-ray source reflected by an optically thick neutral slab. In this model, the parameter R measures the reflection component. If the source is isotropic, R can be linked to the solid angle Ω as $R \simeq \frac{\Omega}{2\pi}$. The value of R depends on the inclination angle i between the perpendicular to the accretion disk and the line of sight. The smaller the inclination angle, the larger the resulting reflection component. The quality of the data does not allow us to constrain both R and i at the same time, so we fixed the inclination angles to $i = 45^\circ$ for all the classes. We used the same value of i for all the classes to characterize the reflection with a single parameter. We note that by doing this R no longer represents $\Omega/2\pi$, and becomes only an indicator of the reflection amplitude.

5.1. Seyfert galaxies

Fitting the spectra of Seyfert 1s, Seyfert 1.5s, and Seyfert 2s with a simple power law yields a reduced chi-squared of $\chi^2_\nu = 1.4$, $\chi^2_\nu \simeq 1.4$, and $\chi^2_\nu \simeq 3.9$, respectively. The null-hypothesis probability is 20%, 18%, and $< 0.1\%$ for Sy1s, Sy1.5s, and Sy2s, respectively.

Applying a cutoff power law improves the fit of both Seyfert 1s and Seyfert 2s at a confidence level of 84% and 99.6%, respectively. Adding a reflection component to the power law model also significantly improves the fit for both Seyfert 1s and

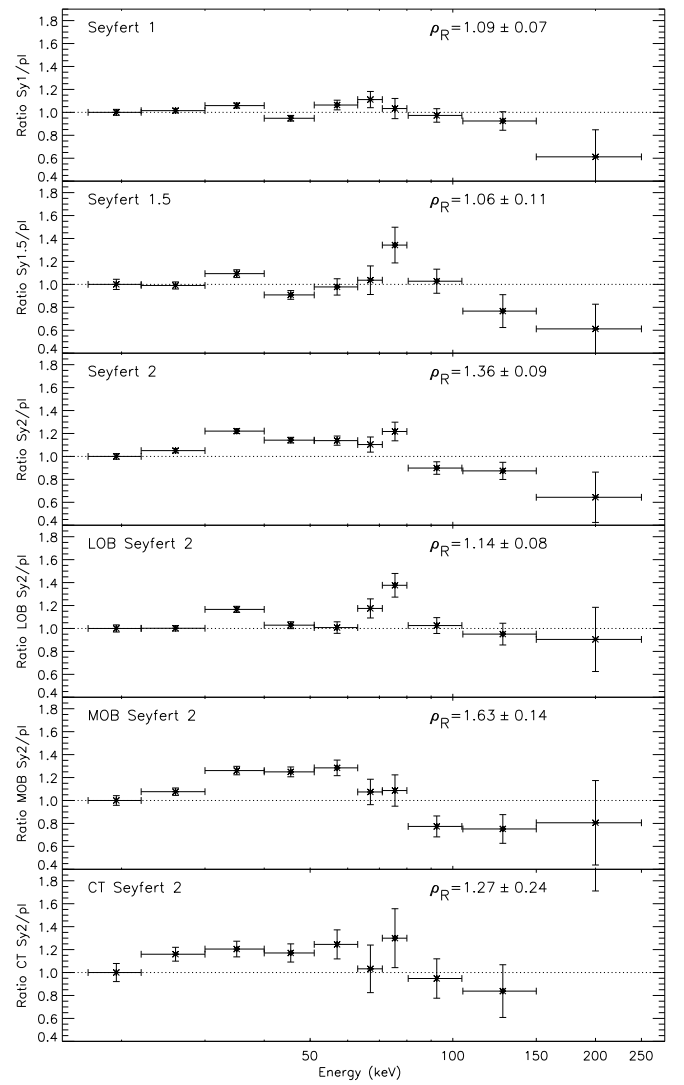


Fig. 12. Ratio between the normalized spectra of Seyfert 1s, Seyfert 1.5s, Compton-thin Seyfert 2, LOB Seyfert 2s, MOB Seyfert 2s, and Compton-thick Seyfert 2s, and a simulated power law spectrum ($\Gamma = 1.9$). The parameter ρ_R is defined in Eq. 2.

Seyfert 2s. The fit to the spectrum of Seyfert 1.5s does not improve significantly by adding any of these features to the baseline power law model. Fitting with different models the spectrum of Seyfert 1.5s, one notes that most of the chi-squared comes from a single bin (71–80 keV, see Appendix B). On the basis of this, and that in Sect. 4 we have shown that the spectra of Seyfert 1s and Seyfert 1.5s are very similar, we use the same models to characterize their spectra. The results of the spectral analysis are reported in Table 3.

Both a high-energy cutoff and a reflection component from neutral matter are thought to play an important role in the hard X-ray emission of Seyfert galaxies, thus in the following we discuss only the results obtained using *pexrav*. Applying this model, we obtained a lower limit to the high-energy cutoff of $E_C \gtrsim 190$ keV, and a reflection normalization of $R \leq 0.4$ for both Seyfert 1s and Seyfert 1.5s. The consistency of these parameters agrees with that found in Sect. 4. Using the same model for the average spectrum of Seyfert 2s, we obtained $E_C = 154^{+185}_{-84}$ keV and $R \leq 2.6$, which confirms the greater curvature observed.

Owing to its low statistics, a simple power law model provides a good fit ($\chi^2_v = 1$) to the stacked spectrum of the ten CT Seyfert 2 galaxies of our sample. Although statistically not required, a cutoff and a reflection component reduce the chi-squared of $\Delta\chi^2 = 3.8$ and $\Delta\chi^2 = 5.1$, respectively. Using *pexrav*, we could not constrain E_C , while we obtained an upper limit to the reflection normalization of $R \leq 11.2$.

A power-law model cannot represent well the hard X-ray spectrum of NLS1s. Adding a cutoff or a reflection component significantly improves the fit, although it is not possible to constrain the two parameters at the same time. We obtained a photon index of $\Gamma = 2.3^{+0.1}_{-0.6}$, a lower limit to the energy of the cutoff of $E_C \geq 53$ keV, and to the reflection parameter of $R \geq 0.1$.

The average photon indices obtained are consistent for the different subsamples of Seyfert galaxies, and have values of $\Gamma \simeq 1.8$, in agreement with previous studies (e.g., Dadina et al. 2008). The spectra of Seyfert 1s, Seyfert 1.5s, Seyfert 2s, CT Seyfert 2s, and NLS1s are shown in Appendix B.

5.2. MOB and LOB Seyfert 2s

Using *pexrav* to fit the spectra of MOB and LOB Sy2s, we confirmed the different curvatures of the spectra of the two subsamples, obtaining values of the reflection parameter of $R \leq 0.5$ and $R = 2.2^{+4.5}_{-1.1}$, for LOB and MOB Sy2s, respectively. The photon indices ($\Gamma \sim 1.8$) and the energies of the cutoff ($E_C^{\text{LOB}} = 425^{+267}_{-120}$ keV and $E_C^{\text{MOB}} = 287^{+105}_{-64}$ keV) obtained by the fit are consistent to within 3σ . The results are reported in Table 4, while the spectra of MOB and LOB Sy2s are shown in Appendix B.

The spectral analysis performed using different models confirms that the average hard X-ray spectrum of LOB Sy2s is more similar to those of Seyfert 1s and Seyfert 1.5s than to that of MOB Sy2s.

5.3. Seyfert 2s with and without PBL

Consistently with what was obtained for the whole sample of Seyfert 2s, the spectra of PBL and NPBL Sy2s cannot be reproduced using solely a power law, but need to be fitted using a more complex model. Adding a high-energy cutoff or a reflection component to the power law significantly improves the fit for both spectra. All the models used give values of the parameters of the two spectra that are consistent to within 3σ , confirming the similarities found by the model-independent analysis. The results of the spectral analysis are reported in Table 5.

6. Reflection in MOB Sy2s

We have shown that the spectrum of MOB Sy2s shows a stronger reflection component than those of LOB Sy2s, Seyfert 1s, and Seyfert 1.5s, and we now investigate the possible causes of this effect.

The spectrum of lightly obscured objects (LOB Sy2s, Sy1s, and Sy1.5s) can be expressed by

$$F(E) = AE^{-\Gamma} e^{-E/E_C} + R(E), \quad (3)$$

where A is the normalization and $R(E)$ the reflection component, which was accounted for using *pexrav*. The observed 20–60 keV bump might be due to a distant (i.e. unabsorbed) reflection component, which becomes more important for MOB Sy2s due to the larger fraction of Compton scattered continuum. This reflector has been associated with the inner wall of the torus, or the

Table 3. Results obtained from the spectral analysis of the average hard X-ray spectra of Seyfert 1s, Seyfert 1.5s, Seyfert 2s, CT Sy2s, and NLS1s. The inclination angle i was fixed to 45° .

Model	Γ	E_C [keV]	R	χ^2/DOF	FTEST
Seyfert 1s					
Power law	$1.97^{+0.05}_{-0.05}$	–	–	11/8	–
Cut-off power law	$1.8^{+0.1}_{-0.2}$	293^{+NC}_{-150}	–	8.2/7	0.17
*Pexrav	$1.96^{+0.04}_{-0.04}$	–	$0.2^{+0.2}_{-0.2}$	9.8/7	0.38
Pexrav	$1.8^{+0.2}_{-0.1}$	340^{+NC}_{-155}	$0.1^{+0.3}_{-0.1}$	8.3/6	0.43
Seyfert 1.5s					
Power law	$1.97^{+0.09}_{-0.08}$	–	–	11.4/8	–
Cut-off power law	$1.9^{+0.1}_{-0.3}$	500^{+310}_{-250}	–	11.3/7	0.81
*Pexrav	$1.97^{+0.05}_{-0.05}$	–	$0.2^{+0.3}_{-0.2}$	11.3/7	0.81
Pexrav	$1.8^{+0.2}_{-0.1}$	332^{+NC}_{-145}	$0.1^{+0.3}_{-0.1}$	11.3/6	0.97
Seyfert 2s					
Power law	$1.93^{+0.03}_{-0.03}$	–	–	31/8	–
Cut-off power law	$1.4^{+0.2}_{-0.2}$	86^{+41}_{-22}	–	8.9/7	< 0.01
*Pexrav	$1.97^{+0.05}_{-0.05}$	–	$2.0^{+3.9}_{-1.2}$	9.3/7	< 0.01
Pexrav	$1.6^{+0.4}_{-0.4}$	154^{+185}_{-84}	$0.4^{+2.2}_{-0.4}$	7.4/6	0.01
CT Seyfert 2s					
Power law	$1.9^{+0.1}_{-0.1}$	–	–	8/8	–
Cut-off power law	$1.5^{+0.2}_{-0.2}$	100^{+NC}_{-51}	–	4.2/7	0.04
*Pexrav	$1.9^{+0.1}_{-0.1}$	–	$1.4^{+9.6}_{-1.2}$	2.7/7	< 0.01
Pexrav	$2.0^{+0.1}_{-0.1}$	NC	$1.5^{+9.7}_{-1.5}$	2.7/6	0.04
Narrow Line Seyfert 1s					
Power law	$2.23^{+0.08}_{-0.08}$	–	–	24.6/8	–
Cut-off power law	$1.7^{+0.2}_{-0.6}$	70^{+43}_{-36}	–	11.6/7	0.03
*Pexrav	$2.28^{+0.08}_{-0.08}$	–	$4.3^{+NC}_{-3.0}$	9.5/7	0.01
Pexrav	$2.3^{+0.1}_{-0.6}$	310^{+NC}_{-257}	$4.2^{+NC}_{-4.1}$	9.5/6	0.06

Notes. NC: the parameter or the 3σ error were not constrained.

*Pexrav: the high-energy cut off was not included, being fixed to its upper limit $E_C = 10^6$ keV.

outer part of the disk. The spectrum of MOB objects can be represented by

$$F(E) = M(E, N_H)AE^{-\Gamma} e^{-E/E_C} + R(E). \quad (4)$$

In the following, we assume that $\Gamma = 1.8$, $E_C = 300$ keV. We first simulated and compared several spectra with the same continuum and reflection component, but with different values of N_H , to see whether absorption might explain the differences observed. The value of R associated with the torus remains unknown (e.g., Gilli et al. 2007 consider a value of $R_T = 0.37$). To obtain an upper limit to the effect, we assumed $R = 1$ (for both LOB and MOB objects), and column densities of $N_H = 7 \times 10^{23} \text{ cm}^{-2}$ and $N_H = 0$ for MOB and LOB objects, respectively. We tested two different values of the inclination angle for MOB Sy2s ($i = 30^\circ$ and $i = 60^\circ$), while we set $i = 60^\circ$ for LOB objects. The parameter $M(E, N_H)$ includes both Compton scattering (through the *cabs* model) and photoelectric absorption (implemented as *wabs*), as given in Eq. 1. In Fig. 13 (*left panel*), we show the ratios obtained comparing the simulated spectra. From the figure, it is evident that a column density of $N_H = 7 \times 10^{23} \text{ cm}^{-2}$ is largely insufficient to explain the observed differences. To provide an excess closer to what is ob-

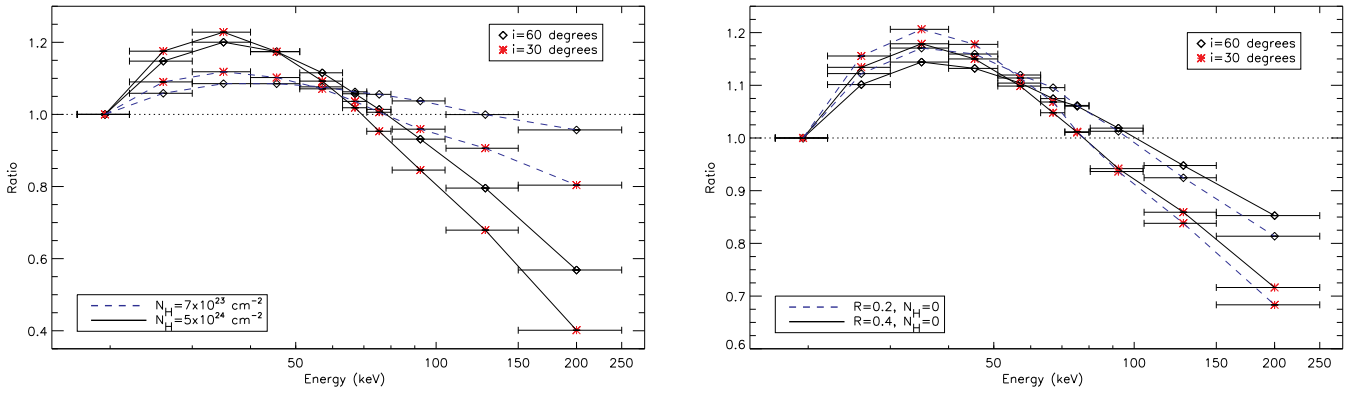


Fig. 13. Ratios of simulated spectra of MOB (Eq. 4) to LOB (Eq. 3) objects. We assumed $\Gamma = 1.8$, $E_C = 300$ keV for the continuum of all spectra. We tested different values of i and N_H ($N_H = 7 \times 10^{23} \text{ cm}^{-2}$ and $N_H = 5 \times 10^{24} \text{ cm}^{-2}$) for the spectrum of MOB Sy2s, assuming $R = 1$ for all the spectra, and $N_H = 0$ for LOB Sy2s (left panel). We tested different values of the reflection parameter ($R = 0.4$ and $R = 0.2$ for LOB objects, fixing $R = 1$ for MOB Sy2s), and of i (only for MOB Sy2s), setting $N_H = 3 \times 10^{23} \text{ cm}^{-2}$ for MOB Sy2s and $N_H = 0$ for LOB Sy2s (right panel).

Table 4. Results obtained from the spectral analysis of the average hard X-ray spectra of MOB and LOB Seyfert 2s. The inclination angle i was fixed to 45° .

Model	Γ	E_C [keV]	R	χ^2/DOF	FTEST
MOB Seyfert 2s					
Power law	$1.94^{+0.05}_{-0.05}$	—	—	45.2/8	—
Cut-off power law	$1.0^{+0.3}_{-0.3}$	47^{+20}_{-11}	—	7.6/7	< 0.01
*Pexrav	$1.95^{+0.05}_{-0.05}$	—	7^{+7}_{-2}	9.8/7	< 0.01
Pexrav	$1.82^{+0.06}_{-0.06}$	287^{+105}_{-64}	$2.2^{+4.5}_{-1.1}$	8.8/6	< 0.01
LOB Seyfert 2s					
Power law	$1.91^{+0.04}_{-0.04}$	—	—	15.9/8	—
Cut-off power law	$1.7^{+0.2}_{-0.1}$	224^{+NC}_{-98}	—	12.8/7	0.23
*Pexrav	$1.91^{+0.04}_{-0.04}$	—	$0.4^{+0.5}_{-0.3}$	13.7/7	0.32
Pexrav	$1.8^{+0.2}_{-0.3}$	425^{+267}_{-120}	$0.2^{+0.3}_{-0.2}$	12.9/6	0.53

Notes. NC: the parameter or the 3σ error were not constrained.

*Pexrav: the high-energy cut off was not included, being fixed to its upper limit $E_C = 10^6$ keV.

served, one would need a value of the column density as large as $N_H = 5 \times 10^{24} \text{ cm}^{-2}$.

We then tested different values of the reflection parameter. From the spectral analysis, we found upper limits of the reflection parameter of $R \leq 0.4$ for Seyfert 1s and Seyfert 1.5s, and of $R \leq 0.5$ for LOB Sy2s. These values are significantly lower than that obtained for MOB Sy2s ($R = 2.2^{+4.5}_{-1.1}$). We simulated and compared spectra obtained using Eqs. 3 and 4, considering different amounts of reflection and absorption for LOB ($R = 0.5$ and $R = 0.2$, $N_H = 0$, $i = 60^\circ$) and MOB ($R = 1$, $N_H = 7 \times 10^{23} \text{ cm}^{-2}$, $i = 60^\circ$ and $i = 30^\circ$) objects. From Fig. 13 (right panel), one can see that a greater unabsorbed reflection component in MOB Seyfert 2s would explain their larger amount of flux in the 20–60 keV energy band with respect to LOB objects.

We fitted the spectrum of MOB Sy2s with Eq. 4 in XSPEC, setting the column density of the absorbing medium to the average value (weighted by the detection significance) of the sample ($N_H = 3 \times 10^{23} \text{ cm}^{-2}$). We first assumed a edge-on reflector

Table 5. Results obtained from the spectral analysis of the average hard X-ray spectra of PBL and NPBL Seyfert 2s. The inclination angle i was fixed to 45° .

Model	Γ	E_C [keV]	R	χ^2/DOF	FTEST
PBL Seyfert 2s					
Power law	$1.94^{+0.03}_{-0.03}$	—	—	23.7/8	—
Cut-off power law	$1.6^{+0.2}_{-0.2}$	136^{+135}_{-48}	—	11.7/7	0.03
*Pexrav	$1.95^{+0.03}_{-0.03}$	—	$1.0^{+0.6}_{-0.4}$	8.5/7	< 0.01
Pexrav	$1.9^{+0.2}_{-0.3}$	803^{+NC}_{-660}	$0.7^{+0.8}_{-0.6}$	8.5/6	0.05
NPBL Seyfert 2s					
Power law	$1.95^{+0.09}_{-0.09}$	—	—	22.9/8	—
Cut-off power law	$1.1^{+0.5}_{-0.5}$	49^{+70}_{-20}	—	13.9/7	0.07
*Pexrav	$1.97^{+0.09}_{-0.09}$	—	$3^{+NC}_{-2.3}$	14.4/7	0.08
Pexrav	$1.9^{+0.1}_{-0.1}$	874^{+NC}_{-548}	$2.9^{+NC}_{-2.3}$	13.7/6	0.21

Notes. NC: the parameter or the 3σ error were not constrained.

*Pexrav: the high-energy cut off was not included, being fixed to its upper limit $E_C = 10^6$ keV.

($i = 60^\circ$), and fixed E_C to different values. The best fit yields $R \geq 2$ and is obtained for $E_C = 300$ keV. The value of the reflection parameter is $R > 1$ even when considering higher values of E_C . Considering a face-on reflector ($i = 30^\circ$), we obtained a lower value of the reflection parameter for $E_C = 300$ keV ($R = 1.1^{+3.5}_{-0.5}$), while we obtained $R \geq 1$ for higher values of E_C . The results of the fits are listed in Table 6.

7. Discussion

We now discuss the average hard X-ray spectra of the different classes of Seyfert galaxies, the differences and similarities between PBL and NPBL Sy2s, the average hard X-ray emission of NLS1s, and all this in the framework of the unified model and the cosmic X-ray background.

Table 6. Results obtained by fitting the spectrum of MOB Seyfert 2s with Eq. 4, fixing N_{H} to the average value of the sample. We tested different values of the cutoff energy and the inclination angle.

E_C [keV]	Γ	R	i	χ^2	DOF
300*	$1.78^{+0.07}_{-0.07}$	3^{+10}_{-1}	60°	9.6	7
	$1.74^{+0.06}_{-0.06}$	2^{+3}_{-1}	45°	9.7	7
	$1.76^{+0.07}_{-0.09}$	$1.3^{+1.8}_{-0.5}$	30°	9.9	7
500*	$1.83^{+0.07}_{-0.07}$	$3.5^{+NC}_{-2.0}$	60°	10.3	7
	$1.82^{+0.06}_{-0.06}$	$2.5^{+7.8}_{-1.5}$	45°	10.3	7
	$1.81^{+0.07}_{-0.07}$	$2.0^{+3.5}_{-1}$	30°	10.4	7
∞^*	$1.99^{+0.06}_{-0.06}$	13^{+NC}_{-10}	60°	11.9	7
	$1.95^{+0.06}_{-0.05}$	$5.3^{+NC}_{-3.7}$	45°	11.8	7
	$1.96^{+0.07}_{-0.07}$	3^{+NC}_{-2}	30°	11.9	7

Notes. NC: 3σ error not constrained; *: parameter fixed.

7.1. Seyfert galaxies: the continuum

From our analysis of the average hard X-ray spectra of Seyfert galaxies, we found that the primary power law emission is similar for both Seyfert 1s and Seyfert 2s, and can be described by a photon index of $\Gamma \simeq 1.8$. Comparing the average spectra to a simulated power law, we found for Sy1s, Sy1.5s and Sy2s only a weak softening in the last energy bin, which might imply that on average the cutoff is at energies $E_C \gtrsim 150$ keV. This was confirmed by the model-dependent spectral analysis, from which we found $E_C \gtrsim 200$ keV, which is consistent with the results of *BeppoSAX* observations (Dadina 2008).

In the thermal Comptonization scenario, the power law emission of AGN is commonly assumed to arise from inverse Comptonization of soft photons in a hot plasma. Within this scenario, the cutoff energy and the photon index are linked to the temperature and the optical depth of the hot plasma responsible for the Comptonization. According to Petrucci et al. (2001), the temperature can be estimated as $kT_e = E_C/2$ for $\tau \lesssim 1$, or $kT_e = E_C/3$ for $\tau \gg 1$, and the three parameters are related by

$$\Gamma - 1 \simeq \left\{ \frac{9}{4} + \frac{m_e c^2}{kT_e \tau (1 + \tau/3)} \right\}^{1/2} - \frac{3}{2}. \quad (5)$$

Using Eq. 5 and the values of the parameters obtained using the *pexrav* model, we calculated the average optical depths of the different classes of Seyferts. For Seyfert 1s and Seyfert 1.5s, we obtained $\tau = 0.8^{+0.6}_{-0.5}$, which is consistent with the values obtained for LOB ($\tau = 0.7^{+0.6}_{-0.4}$) and MOB Seyfert 2s ($\tau_2 = 0.9^{+0.3}_{-0.3}$). The consistency of τ indicates that the average physical characteristics of the Comptonizing medium are similar for different classes of Seyferts, as expected from the UM.

7.2. Seyfert galaxies: the reflection component

The hard X-ray spectrum of Seyfert 2s shows a harder emission in the 20–60 keV band than those of Seyfert 1s and Seyfert 1.5s (Fig. 7). Most of this difference can be ascribed to the contribution of MOB Sy2s (Fig. 9), while LOB Sy2s show characteristics more similar to Seyfert 1s and Seyfert 1.5s (Fig. 10), although still having a $\sim 20\%$ excess in the 30–50 keV band.

The greater reflection of MOB Sy2s cannot be explained solely by the dampening of the continuum caused by absorption, but we have demonstrated that different values of R must also be taken into account (Fig. 13). We have in fact shown that the average value of Seyfert 1/1.5s and LOB Sy2s is $R \leq 0.4$ and $R \leq 0.5$ (Section 5), respectively, while for MOB Sy2s this value is greater ($R > 1$, see Section 6).

From a purely geometrical point of view, and considering the disk as the main reflector, one would expect a greater influence of the reflection component in the spectrum of Seyfert 1s rather than in that of Seyfert 2s, the angle i between the normal to the disk and the observer being smaller. Different luminosity distributions could introduce a bias in our hard X-ray selected sample of MOB Sy2s, with sources having a stronger reflection component being brighter and thus more easily detected. However, the difference between the average luminosities of MOB ($L^{MOB} \simeq 1.7 \times 10^{43} \text{ erg s}^{-1}$) and LOB Sy2s ($L^{LOB} \simeq 2.1 \times 10^{43} \text{ erg s}^{-1}$) is insignificant. Moreover, a KS test results in a probability of $\simeq 86\%$ that the two samples of Seyfert 2s are statistically compatible. Different inclination angles might also play a role in explaining the large reflection of MOB Sy2s, although the average values of i would have to be extreme to account for the observed differences.

A possible explanation is that in MOB Sy2s the putative torus, which is also the dominant reflector, covers a larger fraction of the X-ray source than in lightly obscured objects. A similar geometry was hypothesized by Ueda et al. (2007) to explain the *Suzaku* spectra of SWIFT J0601.9–8636 and SWIFT J0138.6–4001. Further evidence for the existence of these deeply buried AGN was found by Eguchi et al. (2009). Being more absorbed, MOB Sy2s might on average have more matter surrounding the active nucleus, which would be responsible for the larger reflection. Ramos Almeida et al. (2009, 2011) analyzing the mid-infrared emission of Seyfert galaxies found that the clumpy absorbers in Sy2s have larger covering factors ($C_T = 0.95 \pm 0.02$) than those in Sy1s ($C_T = 0.5 \pm 0.1$). Among the 12 Sy2s in their sample, ten have $N_{\text{H}} \gtrsim 10^{23} \text{ cm}^{-2}$, which supports our argument of a larger average covering fraction of the absorber for more obscured sources. The small value of the average reflection parameter of Sy1s and Sy1.5s might imply that on average the reflection from the disk does not play as important a role as that of the absorber.

A value of $R > 1$ is unphysical if related only to the geometry, and might imply that part of the direct emission is blocked by partially covering material, with the transmission efficiency being $\lesssim 1/R$ (Ueda et al. 2007). If the X-ray source is partially covered by Compton-thick material, the reflected component would in fact have a stronger relative influence over the continuum. Krolik & Begelman (1988) showed that a torus with a smooth dust distribution cannot survive close to the AGN, and proposed that the material is distributed in a clumpy structure. Mid-infrared spectra of Seyfert galaxies have been proven to be consistent with the clumpy torus scenario (e.g., Mor et al. 2009). Evidence has been found in the past few years of significant variations in N_{H} , with changes from Compton-thick to Compton-thin states on timescales from weeks (Risaliti et al. 2005) to ~ 10 hours (Risaliti et al. 2009). These variations have been interpreted as eclipses of the X-ray source caused by the BLR. If the BLR lies between the X-ray source and the putative torus, then it could provide the CT clumps needed to deplete the continuum emission. The variations observed in NGC 1365 (Risaliti et al. 2005, 2009) might be common in MOB Sy2s, and the extremely long *INTEGRAL* IBIS/ISGRI observations we used to derive the average spectra might have registered some of them.

The presence of CT clumps might be a common characteristic in the absorbers of Seyfert galaxies, and be responsible, at least in part, for the large reflection observed in MOB Sy2.

Both effects might be at work in MOB Sy2s, with more absorbed objects having on average more matter around the X-ray source, and the distribution of this matter being clumpy.

7.3. Seyfert 2s with and without PBLs

Spectropolarimetric surveys indicate that only 30–50% Seyfert 2s show PBLs (Tran 2001, 2003). The reason for the non-detection of PBLs in all Seyfert 2s is still debated, and it has been hypothesized (Tran 2001, 2003) that NPBL Sy2s might be a different class of Seyfert 2, that possibly lack the BLR and have large-scale characteristics more similar to Seyfert 1s. Deluit (2004) discussed the possible existence of differences in the 15–136 keV spectra of Seyfert 2s with and without PBLs using *BeppoSAX* data, and concluded that the characteristics of PBL Sy2s appear to be more similar to those of Seyfert 1s than NPBL Sy2s. Using a slightly larger sample, but broader energy range and much longer exposures, we analyzed the stacked spectra of PBL and NPBL Sy2s, finding that the two samples do not show any significant spectral differences. The greatest difference between the two samples is their luminosities. The average 17–80 keV luminosity of PBL Sy2s ($L^{\text{PBL}} \simeq 1.9 \times 10^{43} \text{ erg s}^{-1}$) is greater by a factor of $\simeq 3$ than that of NPBL Sy2s ($L^{\text{NPBL}} \simeq 6 \times 10^{42} \text{ erg s}^{-1}$). The luminosity of the [OIII] line is often used as an indicator of the bolometric luminosity of AGN. Collecting data from the literature, we found that the average luminosity of PBL Sy2s ($L_{\text{[OIII]}} = 4.2 \times 10^{40} \text{ erg s}^{-1}$) is still higher than that of NPBL Sy2s ($L_{\text{[OIII]}} = 10^{40} \text{ erg s}^{-1}$). Although this does not give any indication of the intrinsic luminosity of the BLR, it implies that the bolometric luminosity of PBL Sy2s is on average greater than that of NPBL Sy2s, confirming what was found by Tran (2001) and Lumsden & Alexander (2001). We also found that in our sample NPBL Sy2s are on average slightly more absorbed ($N_{\text{H}}^{\text{NPBL}} = 3 \times 10^{23} \text{ cm}^{-2}$) than PBL Sy2s ($N_{\text{H}}^{\text{PBL}} = 1.5 \times 10^{23} \text{ cm}^{-2}$).

The lack of remarkable differences in the hard X-ray spectra of PBL and NPBL Seyfert 2s fits the UM, according to which they are supposed to belong to the same family.

7.4. Narrow-line Seyfert 1s

The 0.1–10 keV spectra of NLS1s are steeper than those of their broad-line counterparts (e.g., Netzer 2001). Owing to this, few of them are detected above 20 keV, and only a handful of NLS1s have been studied so far in the hard X-rays. A sample of five objects was examined using IBIS/ISGRI data (up to 100 keV) by Malizia et al. (2008), who found that their spectra present a continuum significantly steeper than Seyfert 1s and have an average photon index of $\Gamma = 2.6 \pm 0.3$. They interpreted this as being due to a low energy ($E_C \leq 60 \text{ keV}$) of the cutoff. Our sample of 205 Seyfert galaxies contains 14 NLS1s, which makes it the largest ever studied at these energies. In our sample, NLS1s represent $\simeq 15\%$ of the total number of Sy1s and Sy1.5s. This is a much smaller fraction than the $\sim 50\%$ of *ROSAT* soft X-ray selected NLS1s (Grupe 2004), but is consistent with the $\sim 15\%$ obtained from an optically selected sample (Williams et al. 2002). From our analysis, we confirmed that in the hard X-rays the average spectrum of NLS1s is also steeper than those of Sy1s and Sy1.5s, with the spectra clearly diverging above $\sim 40 \text{ keV}$. This might be

due to different values of Γ or to different energies of the cutoff. The fact that up to $\sim 40 \text{ keV}$ the average spectrum of NLS1s is consistent with that of Sy1s favors the hypothesis that the photon indices are consistent, while the energy of the cutoff is lower for NLS1s. This is supported also by the fact that for the objects for which good quality data are available in the soft X-ray band, the values of the photon indices are not significantly different from those of Sy1s (Malizia et al. 2008, Jiménez-Bailón et al. 2008, Winter et al. 2009). Consistent photon indices might be due to a bias towards low values of Γ for our hard X-ray selected sample.

7.5. The unified model of AGN

The fact that the average primary (i.e. excluding the reflected component) hard X-ray emission of Seyfert galaxies is independent of their optical classification, and that PBL and NPBL Sy2s have consistent hard X-ray spectra fits well the zeroth order UM. However, the idea that the anisotropic absorber is the same for all classes does not allow us to easily explain the large reflection seen in Seyfert 2s, and in particular in MOB Seyfert 2s.

A possible geometry might be that in MOB Sy2s the absorbing material covers a large fraction of the X-ray source, which is seen through clumps of Compton-thick material, possibly located in the Compton-thin absorber ($N_{\text{H}} \simeq 10^{23} \text{ cm}^{-2}$). This geometry would also explain the low hard X-ray to [OIV] ratio found in Compton-thin Seyfert 2s by Rigby et al. (2009), and why the luminosity of the Compton-thin Sy2s of our sample is significantly lower than that of Sy1s and Sy1.5s.

7.6. The cosmic X-ray background

The CXB is known to be produced by the integrated emission of unresolved AGN. Thus, to fully understand the spectrum of the CXB, it is extremely important to study the average hard X-ray spectra of Seyfert galaxies. In their CXB synthesis model, Gilli et al. (2007) assumed the disk to be the main reflector, considering a weaker reflection for Seyfert 2s than for Seyfert 1s, and a value of $R = 0.37$ for the unabsorbed reflector. Using these parameters, they hypothesized that, to explain the great amount of flux around $\sim 30 \text{ keV}$, CT Sy2s contribute up to $\sim 30\%$ of the CXB. Risaliti et al. (1999) and Guainazzi et al. (2005) estimated that $\sim 50\%$ of all obscured AGN are CT. However, so far this large amount of CT AGN has not been observed (e.g., Ajello et al. 2008a, Paltani et al. 2008), and only few of them are known. Treister et al. (2009) (hereafter T09) discussed the strong degeneracy between the fraction of CT AGN and the value of the reflection parameter used, finding that for a value of $R \simeq 1$, a lower fraction of CT objects ($\sim 10\%$) is needed. Gandhi et al. (2007) also showed how an enhanced reflection component, due to light bending in their case, might decrease the large fraction of heavily absorbed AGN.

We have shown here that the average spectrum of MOB Sy2s has a strong reflection component, and an average value of $R \gtrsim 1$, although for LOB objects we found a value of R smaller than that used by Gilli et al. (2007). This might imply that obscured objects start to contribute significantly to the peak of the CXB already for $N_{\text{H}} \sim 10^{23} \text{ cm}^{-2}$. To test this, we calculated the average value of R for AGN, and extrapolated the CT AGN density as shown in Fig. 4 of T09. To obtain the average value of R , we used the N_{H} distribution of T09, which considers about the same amount of absorbed (AB, $N_{\text{H}} \geq 10^{23} \text{ cm}^{-2}$, which includes MOB and CT AGN) and LOB ($N_{\text{H}} < 10^{23} \text{ cm}^{-2}$) objects. We showed that the average spectra of CT and MOB Sy2s are

consistent, thus we divided the AGN into two classes, AB and LOB, and used their average reflection parameters (Sect. 5.1) to calculate the average value of R . The value obtained $\bar{R} \sim 1.1$ agrees with that found by T09, and implies that CT AGN have a local density of $\sim 2 \times 10^{-6} \text{ Mpc}^{-3}$, and represent a fraction of $\sim 10\%$ of the total population of AGN.

We fitted the *INTEGRAL* IBIS/ISGRI CXB spectrum of Türler et al. (2010) with the sum of the best-fit models obtained for AB and LOB objects³, fixing all the parameters to the best-fit values found in Sect. 5.1, leaving only the normalization free to vary. Following the N_{H} distribution of T09, and assuming that all the objects contribute equally to the CXB, we forced the two values of the normalization to have the same value ($A_{\text{LOB}} = A_{\text{AB}}$). We set the redshift to $z = 1$. We thus obtained a fit with only one free parameter, the global normalization. This simplified model yields a good fit of the CXB spectrum ($\chi^2 = 13.5$ for 15 DOF) in the 20–200 keV band.

In Fig. 14, we show our fit to the CXB, and the contribution of the different components to the spectrum. Using the N_{H} distribution of T09, we transformed the models of the average spectra of LOB and AB objects into those of the three classes used by Gilli et al. (2007): obscured ($10^{24} \geq N_{\text{H}} \geq 10^{22} \text{ cm}^{-2}$), unobscured ($N_{\text{H}} < 10^{22} \text{ cm}^{-2}$), and CT objects. We added Compton scattering and photoelectric absorption to the model of CT AGN (setting $N_{\text{H}} = 10^{24} \text{ cm}^{-2}$).

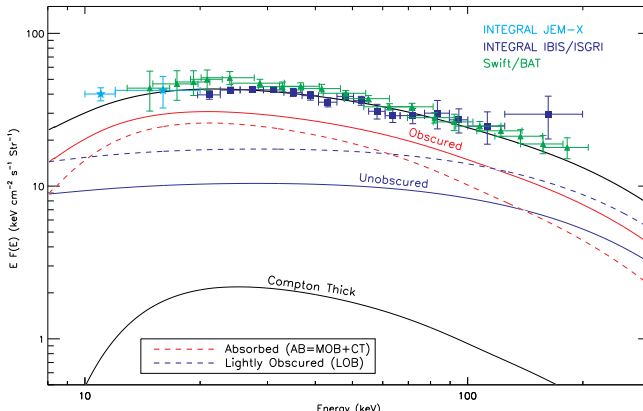


Fig. 14. Fit to the spectrum of the CXB measured by *INTEGRAL* IBIS/ISGRI (squares, Türler et al. 2010). The model used is a combination of our best-fit models for the average spectra of the different classes of objects (AB and LOB), normalizing their ratio using the N_{H} distribution of Treister et al. (2009). We also show the data obtained by *INTEGRAL* JEM-X (stars, Türler et al. 2010) and *Swift* BAT (triangles, Ajello et al. 2008b) above 10 keV.

8. Summary and conclusion

We have presented a study of the average hard X-ray spectra of Seyfert galaxies performed using *INTEGRAL* IBIS/ISGRI data. In the following, we summarize our findings:

- Different classes of Seyfert galaxies have the same average nuclear continuum ($\Gamma \simeq 1.8$, $E_C \gtrsim 200 \text{ keV}$), and their Comptonizing medium has on average a consistent value of the optical depth ($\tau \simeq 0.8$).

- NLS1s have a steeper hard X-ray spectrum than Seyfert 1s and Seyfert 1.5s above $\sim 40 \text{ keV}$. This is likely due to a lower cutoff energy, as proposed by Malizia et al. (2008).
- PBL and NPBL Sy2s have similar hard X-ray spectra, the only difference between the two classes in our incomplete sample being their luminosity.
- Seyfert 2s have on average a stronger reflection component than Seyfert 1s and Seyfert 1.5s.
- Most of the reflection of Seyfert 2s comes from MOB ($10^{23} \text{ cm}^{-2} \leq N_{\text{H}} < 10^{24} \text{ cm}^{-2}$) Sy2s.
- The large amount of reflection observed in MOB Seyfert 2s might be explained by an X-ray source highly covered by the absorbing material. The Compton-thin absorber might contain CT clumps, partially covering the X-ray source.
- The large amount of reflection of MOB Sy2s reduces by a factor of ~ 3 the amount of CT Seyfert 2 needed to explain the CXB peak. Our results are consistent with the fraction of CT AGN being $\sim 10\%$.

Our results, while confirming that the X-ray engine is the same for all classes of Seyfert galaxies, point towards the existence of significant differences in the structure of the medium surrounding the X-ray source between LOB Seyfert galaxies and MOB Seyfert 2s. These differences cannot be solely due to viewing angle dependence, but might imply that there are morphological differences between LOB and MOB AGN.

Appendix A: List of sources

In the following, we list the coordinates, redshifts, detection significances, count rates, column densities, and luminosities of the samples of Seyfert 1s (Table A.1), Seyfert 1.5s (A.2), Compton-thin Seyfert 2s (A.3), CT Seyfert 2s (A.4), and NLS1s (A.5) used for the stacking analysis.

Appendix B: Spectra

In Fig. B.1, we show the average 17–250 keV spectra of Seyfert 1s, Seyfert 1.5s, Seyfert 2s, CT Seyfert 2s, and NLS1s. The parameters of the models used for the fit are reported in Table 3. In Fig B.2, we show the average spectra of MOB and LOB Seyfert 2s. The parameters of the models are reported in Table 4.

Acknowledgements. We thank Marc Türler for providing us the *INTEGRAL* IBIS/ISGRI CXB spectrum, Carlo Ferrigno for his helpful comments on this work, and Piotr Lubinski for his help. We also thank the anonymous referee for his helpful comments. This research has made use of the NASA/IPAC Extragalactic Database (NED) which is operated by the Jet Propulsion Laboratory, of the SIMBAD Astronomical Database, which is operated by the Centre de Données astronomiques de Strasbourg, and of the IGR Sources page maintained by J. Rodriguez & A. Bodaghee⁴.

References

Ajello, M., Rau, A., Greiner, J., et al. 2008a, ApJ 673, 96
 Ajello, M., Greiner, J., Sato, G., et al. 2008b, ApJ 689, 666
 Antonucci, R. R. J., & Miller, J. S. 1985, ApJ 297, 621
 Antonucci, R. R. J. 1993, ARA&A, 31, 473
 Arnaud, K. A. 1996, in: Astronomical Data Analysis Software and Systems V, eds. Jacoby G. and Barnes J., p17, ASP Conf. Series 101

³ In XSPEC, this is translated as `pextrav+pextrav`.

⁴ <http://irfu.cea.fr/Sap/IGR-Sources/>

Table A.1. Coordinates, redshifts, detection significances, count rates, column densities, and luminosities of the Seyfert 1s used for the stacking analysis. Detection significances, count rates, and luminosities are in the 17–80 keV band. The flux of the Crab in the 17–80 keV band is of 278 ct s^{-1} .

Name	RA [h m s]	Dec [° ' "]	z	Det. significance [σ]	Count rate [cts^{-1}]	N_{H} [10^{22} cm^{-2}]	$\log L_{17-80 \text{ keV}}$ [erg s^{-1}]
IGR J02086–1742	02 08 31.4	–17 43 04.8	0.129	7.3	0.31 ± 0.04	$< 0.017^a$	44.78
IGR J02097+5222	02 09 37.7	+52 26 43.6	0.049	13.5	0.56 ± 0.04	0.03^b	44.20
Mrk 590	02 14 33.6	–00 46 00.3	0.027	5.0	0.13 ± 0.03	0.03^c	43.05
Mrk 1040	02 28 14.6	+31 18 39.4	0.016	8.4	0.72 ± 0.09	0.067^d	43.33
RBS 345	02 42 16.0	+05 31 48.0	0.069	5.1	0.23 ± 0.04	–	44.11
ESO 548–01	03 41 54.7	–21 15 28.8	0.014	6.1	0.64 ± 0.11	–	43.17
UGC 3142	04 43 46.9	+28 58 19.0	0.022	13.8	0.58 ± 0.04	1.4^e	43.52
LEDA 168563	04 52 04.7	+49 32 45.0	0.029	11.6	0.51 ± 0.04	$< 0.22^b$	43.70
Ark 120	05 16 11.5	–00 09 00.6	0.033	29.3	0.77 ± 0.03	$< 0.1^c$	43.99
EXO 055620–3820.2	05 58 02.0	–38 20 01.0	0.034	5.6	0.31 ± 0.06	2.57^f	43.62
IRAS 05589+2828	06 02 09.7	+28 28 17.0	0.033	17.5	0.61 ± 0.03	$< 0.04^b$	43.89
SWIFT J0640.4–2554	06 40 10.8	–25 49 48.0	0.026	5.0	0.39 ± 0.08	0.33^f	43.49
IGR J07597–3842	07 59 41.7	–38 43 57.4	0.040	21.8	0.60 ± 0.03	0.05^d	44.05
PG 0804+761	08 10 58.7	+76 02 42.5	0.100	5.0	0.20 ± 0.04	0.023^d	44.37
Fairall 1146	08 38 30.7	–35 59 35.0	0.032	14.0	0.34 ± 0.02	0.1^d	43.61
IGR J09026–4812	09 02 37.3	–48 13 34.1	0.039	21.6	0.37 ± 0.02	0.9^g	43.82
SWIFT J0917.2–6221	09 16 09.4	–62 19 29.5	0.057	12.1	0.34 ± 0.03	0.5^h	44.11
4U 0937–12	09 45 42.1	–14 19 35.0	0.008	17.1	0.99 ± 0.06	1.19^f	42.87
SWIFT J1038.8–4942	10 38 45.0	–49 46 55.0	0.060	9.3	0.25 ± 0.03	1.55^f	44.02
IGR J11457–1827	11 45 41.0	–18 27 29.0	0.033	6.8	0.87 ± 0.13	$\simeq 0^f$	44.05
IGR J12107+3822	12 10 43.4	+38 22 51.6	0.023	5.3	0.17 ± 0.03	–	43.02
IGR J12136–0527	12 13 37.0	–05 26 53.0	0.066	5.3	0.16 ± 0.03	2.0^i	43.91
IGR J12172+0710	12 17 09.0	+07 09 33.0	0.007	8.3	0.22 ± 0.03	0.15^i	42.10
Mrk 50	12 23 24.1	+02 40 44.8	0.023	8.9	0.22 ± 0.02	0.018^d	43.14
NGC 4593	12 39 39.4	–05 20 39.3	0.009	39.7	1.03 ± 0.03	0.02^j	42.99
ESO 323–77	13 06 26.6	–40 24 50.0	0.015	16.6	0.50 ± 0.03	6.0^k	43.12
IGR J13109–5552	13 10 43.1	–55 52 11.7	0.104	15.2	0.31 ± 0.02	$< 0.1^c$	44.60
Mrk 279	13 53 03.5	+69 18 29.2	0.031	5.0	0.64 ± 0.13	0.02^f	43.86
RHS 39	14 19 22.2	–26 38 41.0	0.022	10.4	0.46 ± 0.04	$< 0.05^c$	43.42
IGR J14471–6414	14 46 28.3	–64 16 24.1	0.053	9.7	0.19 ± 0.02	$< 0.1^c$	43.80
IGR J16119–6036	16 11 51.4	–60 37 53.1	0.016	14.8	0.33 ± 0.02	0.1^d	43.00
IGR J16482–3036	16 48 14.9	–30 35 06.1	0.031	29.9	0.62 ± 0.02	0.13^c	43.85
IGR J16558–5203	16 56 05.7	–52 03 41.2	0.054	23.9	0.47 ± 0.02	0.011^c	44.21
IGR J17418–1212	17 41 55.3	–12 11 57.5	0.037	19.4	0.43 ± 0.02	0.1^d	43.84
IGR J18027–1455	18 02 48.0	–14 54 54.8	0.035	23.6	0.42 ± 0.02	0.41^l	43.78
IGR J18259–0706	18 25 57.6	–07 10 22.8	0.037	13.2	0.24 ± 0.02	0.6^c	43.58
ESO 140-43	18 44 54.0	–62 21 52.9	0.014	11.8	0.52 ± 0.04	1.8^e	43.08
IGR J18559+1535	18 56 00.6	+15 37 58.0	0.084	18.3	0.35 ± 0.02	0.7^a	44.46
ESO 141-55	19 21 14.2	–58 40 15.0	0.037	12.7	0.64 ± 0.05	0.004^c	44.01
SWIFT J1933.9+3258	19 33 47.3	+32 54 25.0	0.056	7.0	0.22 ± 0.03	$< 0.04^m$	43.91
IGR J19405–3016	19 40 15.2	–30 15 48.5	0.052	9.0	0.29 ± 0.03	$< 0.1^c$	43.97
RX J2135.9+4728	21 35 54.4	+47 28 28.3	0.025	14.1	0.28 ± 0.02	0.4^c	43.31
IGR J22292+6647	22 29 13.5	+66 46 51.8	0.113	9.7	0.22 ± 0.02	0.2^c	44.52
IGR J23206+6431	23 20 36.8	+64 30 42.8	0.072	9.0	0.15 ± 0.02	0.6^c	43.96

Notes. ^a Rodriguez et al. (2010); ^b Winter et al. (2008) and references therein; ^c Beckmann et al. (2009) and ref. therein;

^d Bodaghee et al. (2007) and ref. therein; ^e Ricci et al. (2010); ^f Winter et al. (2009); ^g Tomsick et al. (2008); ^h Malizia et al. (2007); ⁱ Paltani et al. (2008) and ref. therein; ^j Beckmann et al. (2006) and ref. therein; ^k Jiménez-Bailón et al. (2008); ^l Panessa et al. (2008); ^m Landi et al. (2007a).

Awaki, H., Koyama, K., Inoue, H., & Halpern, J. P. 1991, PASJ, 43, 195
 Barcons, X., Carrera, F. J., & Ceballos, M. T. 2003, MNRAS 346, 897
 Barth, A. J., Tran, H. D., Brotherton, M. S., et al. 1999, AJ 118, 1609
 Bassani, L., Dadina, M., Maiolino, R., et al. 1999, ApJS, 121, 473
 Beckmann, V., Gehrels, N., Shrader, C. R., et al. 2006, ApJ 638, 642
 Beckmann, V., Soldi, S., Ricci, C., et al. 2009, A&A 505, 417
 Bikmaev, I. F., Burenin, R. A., Revnivtsev, M. G., et al. 2008, AstL 34, 653
 Bodaghee, A., Courvoisier, T. J.-L., Rodriguez, J., et al. 2007, A&A 467, 585
 Brightman, M., & Nandra, K. 2011, MNRAS 413, 1206
 Burlon, D., Ajello, M., Greiner, J., et al. 2011, ApJ 728, 58
 Butler, S. C., Tomsick, J. A., Chaty, S., et al. 2009, ApJ 698, 502
 Cai, H.-B., Shu, X.-W., Zheng, Z.-Y., et al. 2010, RAA 10, 427
 Cappi, M., Panessa, F., Bassani, L., et al. 2006, A&A 446, 459
 Caroli, E., Stephen, J. B., Di Cocco, G., et al. 1987, Space Sci. Rev., 45, 349

Table A.2. Coordinates, redshifts, detection significances, count rates, column densities, and luminosities of the Seyfert 1.5s used for the stacking analysis. Detection significances, count rates, and luminosities are in the 17–80 keV band. The flux of the Crab in the 17–80 keV band is of 278 cts s^{-1} .

Name	RA [h m s]	Dec [° ' "]	z	Det. significance [σ]	Count rate [cts s^{-1}]	N_{H} [10^{22} cm^{-2}]	$\log L_{17-80 \text{ keV}}$ [erg s^{-1}]
IGR J00335+6126	00 33 18.4	+61 27 42.4	0.105	9.2	0.14 ± 0.02	0.5^a	44.26
Mrk 1152	01 13 50.1	-14 50 44.1	0.052	5.0	0.47 ± 0.09	2.7^b	44.17
NGC 985	02 34 37.8	-08 47 15.4	0.043	14.9	0.42 ± 0.03	0.6^c	43.96
IGR J03334+3718	03 33 18.8	+37 18 11.4	0.055	5.0	0.18 ± 0.03	–	43.81
4U 0517+17	05 10 45.5	+16 29 55.0	0.017	25.3	0.90 ± 0.04	0.1^c	43.40
SWIFT J0519.5–3140	05 19 35.7	-32 39 25.0	0.013	14.9	0.67 ± 0.05	26.6^e	43.12
MCG+08–11–011	05 54 53.6	+46 26 21.8	0.020	24.9	1.81 ± 0.07	0.18^c	43.93
Mrk 6	06 52 12.3	+74 25 36.8	0.019	16.7	0.74 ± 0.04	10^d	43.50
ESO 209–12	08 01 57.6	-49 46 42.0	0.040	15.8	0.34 ± 0.02	0.1^c	43.81
IGR J09253+6929	09 25 47.6	+69 27 51.5	0.039	5.1	0.29 ± 0.06	8^f	43.72
NGC 3227	10 23 30.6	+19 51 53.7	0.003	17.4	1.88 ± 0.11	6.8^c	42.30
NGC 3516	11 06 47.6	+72 34 08.3	0.009	6.5	1.26 ± 0.19	4^g	43.08
NGC 3783	11 39 01.8	-37 44 18.7	0.009	10.9	2.05 ± 0.19	0.08^b	43.29
IGR J12415–5750	12 41 25.4	-57 50 04.0	0.024	16.2	0.33 ± 0.02	$< 0.11^c$	43.35
IGR J13133–1109	13 13 17.0	-11 08 34.0	0.034	5.0	0.20 ± 0.04	–	43.43
MCG–06–30–015	13 35 53.8	-34 17 44.0	0.008	23.2	0.74 ± 0.03	0.03^c	42.75
IGR J14080–3023	14 08 06.6	-30 23 52.6	0.023	5.0	0.18 ± 0.04	0.03^h	43.05
NGC 5548	14 17 59.7	+25 08 13.4	0.017	7.1	0.49 ± 0.07	0.51^d	43.22
QSO B1419+480	14 21 29.6	+47 47 26.0	0.072	5.2	0.25 ± 0.05	0.5^i	44.18
PG 1501+106	15 04 01.2	+10 26 16.2	0.036	7.2	0.49 ± 0.07	3.9^j	43.87
SWIFT J1930.5+3414	19 30 13.7	+34 10 52.0	0.062	8.8	0.28 ± 0.03	27.5^e	44.10
NGC 6814	19 42 40.4	-10 19 24.0	0.005	25.9	0.79 ± 0.03	$< 0.05^d$	42.37
SWIFT J2009.0–6103	20 08 47.0	-61 05 48.0	0.015	7.6	0.61 ± 0.08	4.53^e	43.21
Mrk 509	20 44 09.8	-10 43 24.7	0.035	16.0	1.12 ± 0.07	$< 0.01^d$	44.21
1RXS J211928.4+333259	21 19 35.5	+33 33 03.6	0.051	9.8	0.29 ± 0.03	–	43.95
1RXS J213944.3+595016	21 39 42.7	+59 49 37.2	0.114	5.5	0.13 ± 0.02	–	44.30
1H 2251–179	22 54 05.9	-17 34 55.3	0.064	9.5	1.12 ± 0.12	$< 0.19^d$	44.73
NGC 7469	23 03 15.8	+08 52 25.9	0.017	10.3	0.78 ± 0.08	0.061^c	43.42
MCG–02–58–022	23 04 43.5	-08 41 08.6	0.047	8.2	0.71 ± 0.09	$< 0.08^d$	44.27

Notes. ^a Beckmann et al. (2009) and ref. therein; ^b Fiore et al. (1997); ^c Bodaghee et al. (2007) and ref. therein; ^d Beckmann et al. (2006) and ref. therein; ^e Winter et al. (2009) and ref. therein; ^f Rodriguez et al. (2008); ^g Guainazzi et al. (2002); ^h Landi et al. (2010); ⁱ Barcons et al. (2003); ^j Longinotti et al. (2010).

Courvoisier, T. J.-L., Walter, R., Beckmann, V., et al. 2003, A&A, 411, 53

Dadina, M. 2007, A&A 461, 1209

Dadina, M. 2008, A&A 485, 417

Deluit, S. & Courvoisier, T. J.-L. 2003, A&A 399, 77

Deluit, S. J. 2004, A&A 415, 39

Della Ceca, R., Severgnini, P., Caccianiga, A. et al. 2008, MmSAI 79, 65

Ebisawa, K., Bourban, G., Bodaghee, A., et al. 2003, A&A 411L, 59

Eguchi, S., Ueda, Y., Terashima, Y., et al. 2009, ApJ 696, 1657

Fiore, F., Matt, G., Nicastro, F. 1997, MNRAS 284, 731

Fiore, F., Giommi, P., Vignali, C., et al. 2001, MNRAS 327, 771

Gandhi, P., Fabian, A. C., Suebsu Wong, T., et al. 2007, MNRAS 382, 1005

Gilli, R., Comastri, A., & Hasinger, G. 2007, A&A 463, 79

Grupe, D., Wills, B. J., Wills, D. et al. 1998, A&A 333, 827

Grupe, D., Beuermann, K., Mannheim, K., et al. 1999, A&A 350, 805

Grupe, D., & Mathur, S. 2004, ApJ 606, 41

Grupe, D. 2004, AJ 127, 1799

Grupe, D., Komossa, S., Leighly, K. M., et al. 2010, ApJS 187, 64

Greenhill, L. J., Tilak, A., Madejski, G. 2008, ApJ 686, L13

Gu, Q., & Huang, J. 2002, ApJ 579, 205

Guainazzi, M., Marshall, W., & Parmar, A. N. 2002, MNRAS 323, 75

Guainazzi, M., Rodriguez-Pascual, P., Fabian, A. C., et al. 2004, MNRAS 355, 297

Guainazzi, M., Matt, G., & Perola, G. C. 2005, A&A 444, 119

Haardt, F., & Maraschi, L. 1991, ApJ 380, L51

Haardt, F., & Maraschi, L. 1993, ApJ 413, 507

Heckman, T. M. 1980, A&A 87, 152

Ho, L. C. 2008, ARAA 46, 475

Jiménez-Bailón, E., Guainazzi, M., Matt, G., et al. 2008, RMxAC 32, 131

Krolik, J. H., & Begelman, M. C. 1988, ApJ 329, 702

Landi, R., Masetti, N., Morelli, L., et al. 2007, ApJ 669, 109

Landi, R., Malizia, A., Masetti, N., et al. 2007, Atel 1274

Landi, R., Bassani, L., Malizia, A. et al. 2010, MNRAS 403, 945

Lebrun, F., Leray, J. P., Lavocat, P., et al. 2003, A&A 411, L141

Longinotti, A. L., Costantini, E., Petrucci, P. O., et al. 2010, A&A 510, 92

Lumsden, S. L., Alexander, D. M. 2001, MNRAS 328L, 32

Magdziarz, P., & Zdziarski, A. A. 1995, MNRAS 273, 873

Malizia, A., Bassani, L., Stephen, J. B. 2003, ApJ 589L, 17

Malizia, A., Landi, R., Bassani, L., et al. 2007, ApJ 668, 81

Malizia, A., Bassani, L., Bird, A. J., et al. 2008, MNRAS 389, 1360

Malizia, A., Bassani, L., Panessa, F., et al. 2009, MNRAS 394, L121

Maoz, D., Nagar, N. M., Falcke, H., et al. 2005, ApJ 625, 699

Maoz, D. 2007, MNRAS 377, 1696

Masetti, N., Parisi, P., Palazzi, E., et al. 2009, A&A 495, 121

Miller, J. S., & Antonucci, R. R. J. 1983, ApJ 271, L7

Moran, E. C., Halpern, J. P., Bothun, G. D., et al. 1992, AJ 104, 990

Morrison, R., & McCammon, D. 1983, ApJ 270, 119

Mor, R., Netzer, H., Elitzur, M. 2009, ApJ 705, 298

Nagao, T., Murayama, T., & Taniguchi, Y. 2000, ApJ 549, 155

Narayan, R. 2005, Ap&SS 300, 177

Netzer, H. 2000, NewAR 44 477

Osterbrock, D. E., & Koski, A. T. 1976, MNRAS 176, 61

Paltani, S., Walter, R., McHardy, I. M., et al. 2008, A&A 485 707

Panessa, F., & Bassani, L. 2002, A&A 394, 435

Panessa, F., Bassani, L., De Rosa, A., et al. 2008, A&A 483, 151

Pappa, A., Georgantopoulos, I., Stewart, G. C., & Zezas, A. L. 2001, MNRAS, 326, 995

Petrucci, P. O., Haardt, F., Maraschi, L., et al. 2001, ApJ 556, 716

Pian, E., Romano, P., Maoz, D., et al. 2010, MNRAS 401, 677

Pfeerkorn, F., Boller, Th., & Rafanelli, P. 2001, A&A 368, 797

Ramos Almeida, C., Levenson, N. A., Rodriguez Espinosa, J. M., et al. 2011, ApJ 702, 1127

Ramos Almeida, C., Levenson, N. A., Alonso-Herrero, A., et al. 2011, ApJ 731, 92

Rees, M. J. 1984, ARA&A 22, 471

Ricci, C., Beckmann, V., Audard, M., et al. 2010, A&A 518, 47

Rigby, J. R., Diamond-Stanic, A. M., & Aniano, G., 2009, ApJ 700, 1878

Risaliti, G., Maiolino, R., & Salvati, M. 1999, ApJ 522, 157

Risaliti, G., Gilli, R., Maiolino, R., et al. 2000, A&A 357, 13

Risaliti, G., Elvis, M., Fabbiano, G., et al. 2005, ApJ 623, L93

Risaliti, G., Salvati, M., Elvis, M., et al. 2009, MNRAS 393, L1

Rodriguez, J., Tomsick, J. A., & Chaty, S. 2008, A&A 482, 731

Rodriguez, J., Tomsick, J. A., & Bodaghee, A. 2010, arXiv1003.3741

Rovilos, E., Georgantopoulos, I., Tzanavaris, P., et al. 2009, A&A 502, 85

Shu, X. W., Wang, J. X., Jiang, P., et al. 2007, ApJ 657, 167

Tomsick, J. A., Chaty, S., Rodriguez, J., et al. 2008, ApJ 685, 1143

Tran, H. D. 2001, ApJ 554, L19

Tran, H. D. 2003, ApJ 583, 632

Treister, E., Urry, C. M., & Virani, S. 2009, ApJ 696, 110

Türler, M., Chernyakova, M., Courvoisier, T. J.-L., et al. 2010, A&A 512, 49

Ubertini, P., Lebrun, F., Di Cocco, G., et al. 2003, A&A 411, L131

Ueda, Y., Eguchi, S., Terashima, Y. et al. 2007, ApJ 664, L79

Veron-Cetty, M.P.& Veron, P.2010, A&A in press

Vignati, P., Molendi, S., Matt, G., et al. 1999, A&A 349, L57

Walter, R. & Cabral, N., 2009 A&A 497, 97

Williams, R. J., Pogge, R. W., Mathur, S. 2002, AJ 124, 3042

Winkler, C., Courvoisier, T. J.-L., Di Cocco, G., et al. 2003, A&A, 411, L1

Winter L. M., Mushotzky R. F., Tueller, J., et al. 2008, ApJ 674, 686

Winter L. M., Mushotzky R. F., Reynolds, C. S., et al. 2009, ApJ 690, 1322

Zdziarski, A. A., Johnson, W. N., Done, C., et al. 1995, ApJ 438, 63

Zhang, W. M., Soria, R., Zhang, S. N., et al. 2009, ApJ 699, 281

Table A.3. Coordinates, redshifts, detection significances, count rates, column densities, and luminosities of the Seyfert 2s used for the stacking analysis. Detection significances, count rates, and luminosities are in the 17–80 keV band. The flux of the Crab in the 17–80 keV band is of 278 ct s^{-1} .

Name	RA [h m s]	Dec [° ' "]	z	Det. significance [σ]	Count rate [ct s^{-1}]	N_{H} [10^{22} cm^{-2}]	PBL	$\log L_{17-80\text{keV}}$ [erg s^{-1}]
IGR J00040+7020	00 04 01.5	+70 19 16.5	0.096	9.4	0.18 ± 0.02	3 ^a	—	44.29
IGR J00254+6822	00 25 31.4	+68 21 41.3	0.012	12.2	0.21 ± 0.02	40 ^b	—	42.55
Mrk 348	00 48 47.1	+31 57 25.1	0.014	23.2	1.59 ± 0.07	30 ^b	Yes ¹	43.56
NGC 526	01 23 54.2	-35 03 55.0	0.019	6.5	0.69 ± 0.11	1.6 ^c	—	43.47
ESO 297-18	01 38 37.2	-40 00 40.7	0.025	9.6	0.76 ± 0.08	42 ^b	—	43.75
IGR J01528-0326	01 52 48.9	-03 26 51.0	0.017	9.1	0.26 ± 0.03	14 ^b	—	42.95
NGC 788	02 01 06.5	-06 48 55.9	0.013	37.4	0.94 ± 0.03	< 0.02 ^b	Yes ²	43.27
Mrk 1018	02 06 08.2	-00 17 02.4	0.043	8.2	0.22 ± 0.03	0.03 ^d	—	43.68
IGR J02343+3229	02 34 19.9	+32 30 20.0	0.016	10.5	0.75 ± 0.07	2.2 ^b	—	43.35
IGR J02501+5440	02 50 41.8	+54 42 15.1	0.015	7.1	0.29 ± 0.04	< 70 ^e	—	42.89
IGR J02524-0829	02 52 23.3	-08 30 38.0	0.017	5.1	0.18 ± 0.04	12 ^f	—	42.79
NGC 1142	02 55 12.3	-00 11 01.7	0.029	25.0	1.03 ± 0.04	45 ^b	No ³	44.01
NGC 1194	03 03 46.1	-01 08 49.2	0.013	6.7	0.34 ± 0.05	1 ^g	—	42.83
SWIFT J0318.7+6828	03 19 02.4	+68 25 48.0	0.090	5.1	0.24 ± 0.05	4.1 ^h	—	44.36
LEDA 15023	04 23 48.2	+04 08 42.0	0.046	8.4	0.36 ± 0.04	—	No ¹	43.95
SWIFT J0444.1+2813	04 44 09.0	+28 13 00.0	0.011	7.4	0.33 ± 0.04	3.39 ^h	—	42.67
SWIFT J0453.4+0404	04 53 31.0	+04 02 02.4	0.029	9.6	0.27 ± 0.03	—	—	43.43
ESO 33-2	04 55 59.6	-75 32 26.0	0.019	8.7	0.35 ± 0.04	0.1 ^c	—	43.17
SWIFT J0505.7-2348	05 05 45.7	-23 51 14.0	0.035	14.8	0.86 ± 0.06	6.57 ^h	—	44.09
NGC 2110	05 52 11.4	-07 27 22.4	0.007	48.5	2.4 ± 0.05	4.3 ^b	Yes ²	43.14
IGR J06239-6052	06 23 45.6	-60 58 45.0	0.041	6.0	0.31 ± 0.05	20 ^b	—	43.78
LEDA 96373	07 26 26.3	-35 54 21.0	0.029	5.9	0.39 ± 0.07	7 ⁱ	—	43.59
IGR J07565-4139	07 56 19.6	-41 37 42.1	0.021	9.3	0.23 ± 0.02	1.1 ^c	—	43.08
SWIFT J0920.8-0805	09 20 46.3	-08 03 21.9	0.020	6.8	0.56 ± 0.08	11.4 ^h	—	43.42
MCG-05-23-016	09 47 40.2	-30 56 54.0	0.008	39.4	2.16 ± 0.06	1.6 ^c	Yes ²	43.21
NGC 3081	09 59 29.5	-22 49 34.6	0.007	15.7	0.95 ± 0.06	66 ^b	Yes ²	42.74
SWIFT J1009.3-4250	10 09 48.3	-42 48 40.4	0.032	15.6	0.55 ± 0.03	30 ^b	—	43.82
IGR J10404-4625	10 40 22.3	-46 25 24.7	0.024	12.4	0.45 ± 0.04	3 ^b	—	43.48
SWIFT J1049.4+2258	10 49 30.9	+22 57 51.9	0.033	5.1	0.42 ± 0.08	42 ^j	—	43.73
SWIFT J1200.8+0650	12 00 57.9	+06 48 23.1	0.036	9.8	0.32 ± 0.03	9.3 ^j	—	43.69
IGR J12026-5349	12 02 47.6	-53 50 07.7	0.028	25.1	0.57 ± 0.02	2.2 ^c	—	43.72
NGC 4074	12 04 32.6	+20 14 56.4	0.022	5.9	0.29 ± 0.05	30 ^h	No ⁴	43.22
NGC 4138	12 09 29.9	+43 41 06.0	0.003	8.6	0.30 ± 0.04	8 ^b	—	41.50
NGC 4258	12 18 57.5	+47 18 14.3	0.002	5.5	0.23 ± 0.04	8.7 ^b	No ⁵	41.03
NGC 4395	12 25 48.8	+33 32 49	0.001	9.5	0.29 ± 0.03	0.15 ^b	—	40.53
NGC 4507	12 35 36.5	-39 54 33.3	0.012	49.6	2.29 ± 0.05	29 ^b	Yes ¹	43.59
SWIFT J1238.9-2720	12 38 54.5	-27 18 28.0	0.024	11.5	1.06 ± 0.09	60 ^b	—	43.86
IGR J12391-1612	12 39 06.3	-16 10 47.1	0.036	11.2	0.55 ± 0.05	3 ^b	—	43.92
IGR J12482-5828	12 47 57.8	-58 29 59.1	0.028	6.7	0.13 ± 0.02	0.3 ⁱ	—	43.08
ESO 323-32	12 53 20.4	-41 38 13.8	0.016	6.8	0.23 ± 0.03	7 ^b	—	42.84
NGC 4941	13 04 13.1	-05 33 05.7	0.003	6.5	0.19 ± 0.03	45 ^k	No ¹	41.30
MCG-03-34-064	13 22 24.5	-16 43 42.9	0.017	6.0	0.40 ± 0.07	41 ^h	Yes ²	43.13
NGC 5252	13 38 16.0	+04 32 32.5	0.022	42.1	1.40 ± 0.03	0.68 ^b	Yes ¹	43.90
Mrk 268	13 41 11.1	+30 22 41.2	0.041	8.4	0.34 ± 0.04	30 ^e	No ⁴	43.83
1AXG J135417-3746	13 54 15.4	-37 46 33.0	0.052	8.3	0.22 ± 0.03	1.6 ^l	—	43.85
IGR J14175-4641	14 17 03.9	-46 41 39.1	0.076	10.4	0.24 ± 0.02	—	—	44.21
IGR J14471-6319	14 47 14.7	-63 17 19.6	0.038	8.5	0.16 ± 0.02	2 ^b	—	43.43
IGR J14561-3738	14 56 08.2	-37 38 53.8	0.024	7.9	0.18 ± 0.02	—	—	43.09
IGR J14579-4308	14 57 41.3	-43 07 57.0	0.016	17.1	0.36 ± 0.02	20 ^b	—	43.04
ESO 328-36	15 14 47.2	-40 21 35	0.024	7.9	0.17 ± 0.02	—	—	43.06
IGR J15161-3827	15 15 59.3	-38 25 48.3	0.036	5.0	0.11 ± 0.02	22 ^m	—	43.22
NGC 5995	15 48 25.0	-13 45 28.0	0.025	8.3	0.39 ± 0.05	0.7 ^b	Yes ¹	43.46
IGR J15539-6142	15 53 35.2	-61 40 55.4	0.015	9.8	0.21 ± 0.02	18 ^b	—	42.74
SWIFT J1650.5+0434	16 50 35.3	+04 35 42.0	0.032	5.4	0.27 ± 0.05	—	—	43.51
NGC 6300	17 16 59.2	-62 49 11.0	0.003	32.4	1.11 ± 0.03	22 ^b	No ¹	42.07
IGR J17513-2011	17 51 13.0	-20 12 14.5	0.047	22.3	0.31 ± 0.01	0.6 ^b	—	43.91
IGR J18244-5622	18 24 19.5	-56 22 08.7	0.017	14.4	0.56 ± 0.04	14 ^b	—	43.28
Fairall 49	18 36 58.1	-59 24 08.0	0.019	5.2	0.22 ± 0.04	0.01 ⁿ	Yes ²	42.97
ESO 103-35	18 38 20.3	-65 25 41.0	0.013	26.2	1.19 ± 0.05	21.6 ^h	—	43.37
IGR J19077-3925	19 07 38.6	-39 25 37.2	0.073	9.8	0.27 ± 0.03	—	—	44.23
IGR J19473+4452	19 47 19.4	+44 49 42.4	0.053	11.2	0.33 ± 0.03	11 ^b	—	44.04
IGR J20216+4359	20 21 48.1	+44 00 32.0	0.017	8.3	0.17 ± 0.02	13 ^o	—	42.76
IGR J20286+2544	20 28 34.9	+25 43 59.7	0.013	19.1	0.66 ± 0.03	42 ^b	—	43.12
Mrk 520	22 00 30.2	+10 36 10.8	0.028	7.6	0.75 ± 0.10	2.4 ^h	—	43.84
NGC 7172	22 02 01.7	-31 52 18.0	0.008	19.1	1.31 ± 0.07	9 ^b	No ¹	42.99
NGC 7314	22 35 46.1	-26 03 01.7	0.005	5.1	0.43 ± 0.09	0.12 ^b	Yes ¹	42.10
IGR J23308+7120	23 30 37.3	+71 22 44.8	0.037	5.0	0.11 ± 0.02	6 ^b	—	43.25
IGR J23524+5842	23 52 22.0	+58 45 31.5	0.162	11.5	0.18 ± 0.02	6 ^b	—	44.75

Notes. References for the column density: ^a Landi et al. (2007b); ^b Beckmann et al. (2009) and ref. therein; ^c Bodaghee et al. (2007)

and ref. therein; ^d Pfefferkorn et al. (2001); ^e Masetti et al. (2008); ^f Rodriguez et al. (2010); ^g Greenhill et al. (2008); ^h Winter et al. (2009)

and ref. therein; ⁱ Landi et al. (2010); ^j Winter et al. (2008) and ref. therein; ^k Paltani et al. (2008); ^l Risaliti et al. (2000);

^m Rodriguez et al. (2008); ⁿ Dadina et al. (2007); ^o Bikmaev et al. (2008).

References for the PBL. ¹ Shu et al. 2007 and ref. therein; ² Veron-Cetty & Veron 2010 and ref. therein; ³ Cai et al. 2010;

⁴ Nagao et al. 2000; ⁵ Barth et al. 1999.

Table A.4. Coordinates, redshifts, detection significances, count rates, column densities, and luminosities of the Compton-thick Seyfert 2s used for the stacking analysis. Detection significances, count rates, and luminosities are in the 17–80 keV band. The flux of the Crab in the 17–80 keV band is of 278 ct s^{-1} .

Name	RA [h m s]	Dec [° ' "]	z	Det. significance [σ]	Count rate [cts^{-1}]	N_{H} [10^{22} cm^{-2}]	$\log L_{17-80 \text{ keV}}$ [erg s^{-1}]
NGC 1068	02 42 40.8	-00 00 48.4	0.003	14.0	0.45 ± 0.03	150 ^a	41.91
SWIFT J0601.9–8636	06 05 39.1	-86 37 52.0	0.006	7.3	0.40 ± 0.06	101 ^b	42.40
Mrk 3	06 15 36.3	+71 02 14.9	0.014	31.3	1.43 ± 0.05	110 ^c	43.70
NGC 3281	10 31 52.1	-34 51 13.3	0.011	12.0	0.78 ± 0.07	151 ^d	43.26
IGR J13091+1137	13 09 05.6	+11 38 02.9	0.025	14.8	0.51 ± 0.03	90 ^c	43.73
NGC 5643	14 32 41.3	-44 10 24.0	0.003	9.2	0.20 ± 0.02	$60 - 100^e$	41.50
Mrk 477	14 40 38.1	+53 30 15.9	0.037	5.8	0.44 ± 0.07	$> 100^f$	44.09
NGC 5728	14 42 23.3	-17 16 51.6	0.009	13.6	0.80 ± 0.06	210 ^a	43.12
IGR J16351–5806	16 35 13.2	-58 04 49.7	0.009	12.9	0.28 ± 0.02	$> 150^g$	42.69
NGC 7582	23 18 23.5	-42 22 14.1	0.005	5.5	1.20 ± 0.20	160 ^a	42.77

Notes. ^a Della Ceca et al. (2008) and ref. therein; ^b Ueda et al. (2007); ^c Beckmann et al. (2006) and ref. therein;

^d Bodaghee et al. (2007) and ref. therein; ^e Guainazzi et al. (2004); ^f Bassani et al. (1999); ^g Malizia et al. (2009).

Table A.5. Coordinates, redshifts, detection significances, count rates, column densities, and luminosities of the Narrow Lines Seyfert 1s used for the stacking analysis. Detection significances, count rates, and luminosities are in the 17–80 keV band. The flux of the Crab in the 17–80 keV band is of 278 ct s^{-1} .

Name	RA [h m s]	Dec [° ' "]	z	Det. significance [σ]	Count rate [cts^{-1}]	N_{H} [10^{22} cm^{-2}]	$\log L_{17-80 \text{ keV}}$ [erg s^{-1}]
1H 0323+342	03 24 41.2	+34 10 45.9	0.063	5.9	0.20 ± 0.03	0.1 ^a	43.97
Mrk 110	09 25 12.9	+52 17 10.5	0.035	5.0	0.86 ± 0.17	0.019 ^a	44.09
NGC 4051	12 03 09.6	+44 31 53.2	0.002	13.6	0.47 ± 0.03	$< 0.02^b$	41.34
Mrk 766	12 18 26.6	+29 48 45.6	0.013	7.7	0.26 ± 0.03	0.8 ^c	42.71
NGC 4748	12 52 12.0	-13 25 48.0	0.014	5.2	0.16 ± 0.03	$\simeq 0^d$	42.57
Mrk 783	13 02 58.8	+16 24 27.5	0.067	7.3	0.25 ± 0.03	0.046 ^a	44.12
NGC 5506	14 13 14.9	-03 12 27.0	0.007	47.2	2.7 ± 0.06	3.4 ^b	43.19
IGR J14552–5133	14 55 17.9	-51 34 13.3	0.016	12.5	0.25 ± 0.02	0.1 ^a	42.88
IRAS 15091–2107	15 11 54.0	-21 21 21.6	0.044	5.3	0.22 ± 0.04	0.7 ^e	43.70
IGR J16185–5928	16 18 26.4	-59 28 45.3	0.035	10.7	0.23 ± 0.02	$< 0.1^f$	43.52
IGR J16385–2057	16 38 31.1	-20 55 25.0	0.027	7.7	0.26 ± 0.03	0.21 ^g	43.35
IGR J19378–0617	19 37 33.1	-06 13 04.0	0.010	11.2	0.32 ± 0.03	$\simeq 0^h$	42.58
ESO 399–20	20 06 57.2	-34 32 54.0	0.025	6.5	0.23 ± 0.04	0.048 ^a	43.23
IGR J21277+5656	21 27 45.9	+56 56 34.4	0.014	24.2	0.52 ± 0.02	0.1 ^a	43.08

Notes. ^a Bodaghee et al. (2007) and ref. therein; ^b Beckmann et al. (2009) and ref. therein;

^c Beckmann et al. (2006) and ref. therein; ^d Grupe et al. (1998); ^e Jiménez-Bailón et al. (2008);

^f Malizia et al. (2008); ^g Rodriguez et al. (2008); ^h Malizia et al. (2008).

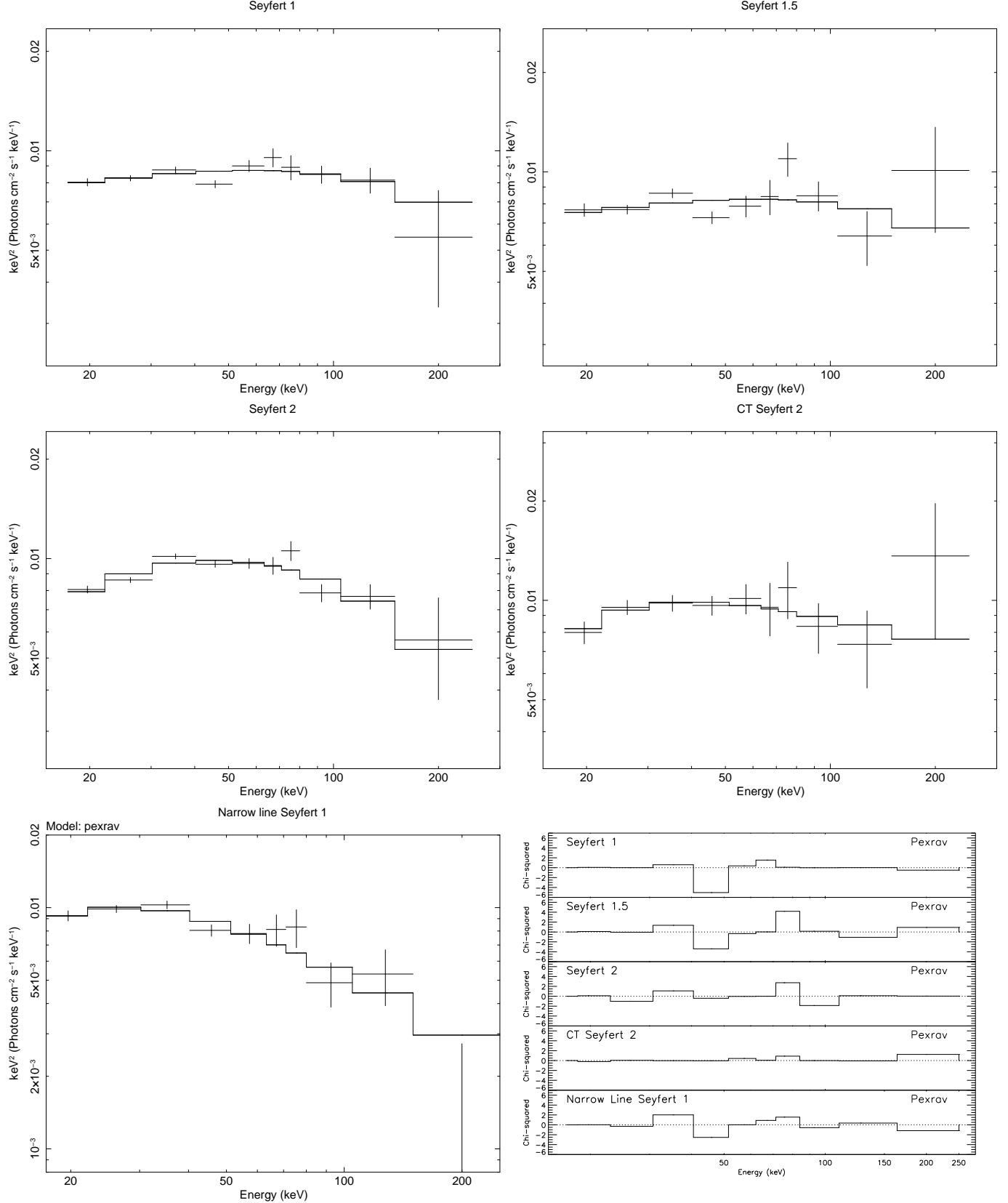


Fig. B.1. Spectra of different classes of AGN obtained using the *pexrav* model. We also show the contributions to the χ^2 relative to the best fits. The results of the spectral analysis are reported in Table 3.

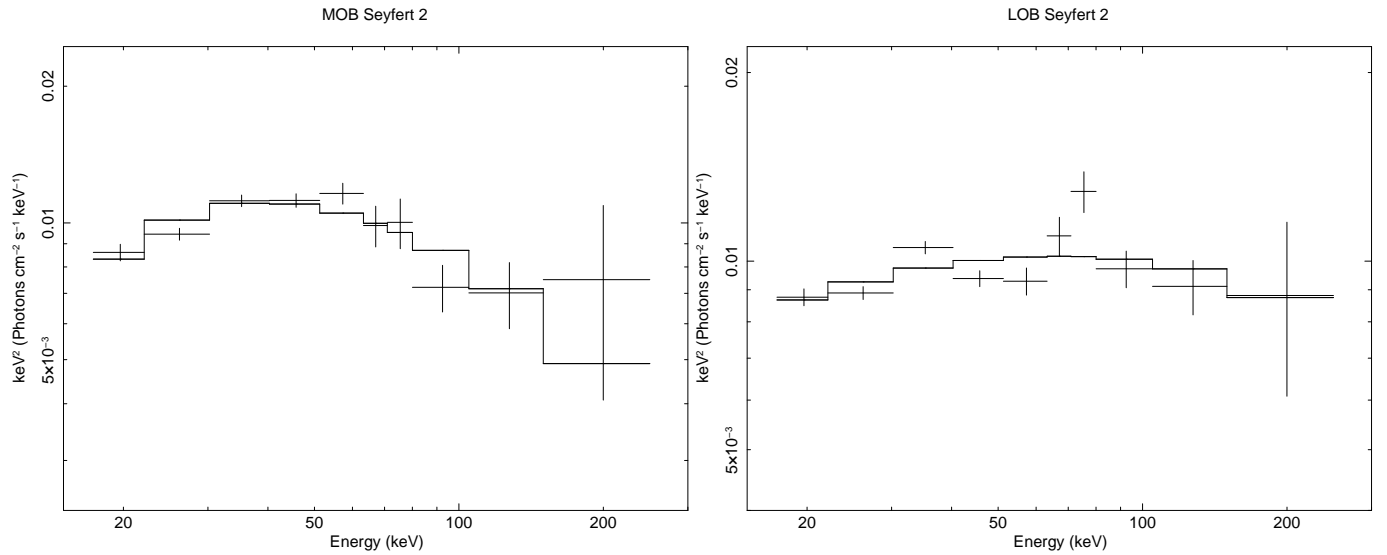


Fig. B.2. Spectra of MOB (left panel) and LOB (right panel) Seyfert 2s, the model used is a cutoff power law plus a reflection component from neutral matter (*pexrav*). The results of the analysis are reported in Table 4.